

2008

Nonlinear materials characterization with femtosecond laser pulses

Geoffrey Drake Jenkins
University of Dayton

Follow this and additional works at: https://ecommons.udayton.edu/graduate_theses

Recommended Citation

Jenkins, Geoffrey Drake, "Nonlinear materials characterization with femtosecond laser pulses" (2008).
Graduate Theses and Dissertations. 3526.
https://ecommons.udayton.edu/graduate_theses/3526

This Thesis is brought to you for free and open access by the Theses and Dissertations at eCommons. It has been accepted for inclusion in Graduate Theses and Dissertations by an authorized administrator of eCommons. For more information, please contact mschlange1@udayton.edu, ecommons@udayton.edu.

**NONLINEAR MATERIALS CHARACTERIZATION WITH
FEMTOSECOND LASER PULSES**

Thesis

Submitted to

The School of Engineering of the
UNIVERSITY OF DAYTON

In Partial Fulfillment of the Requirements for

The Degree

Master of Science in Electro-Optics

by

Geoffrey Drake Jenkins

UNIVERSITY OF DAYTON

Dayton, Ohio

May 2008

NONLINEAR MATERIALS CHARACTERIZATION WITH FEMTOSECOND LASER PULSES

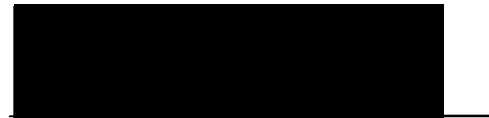
APPROVED BY:



Peter E. Powers, Ph. D.
Advisory Committee Chairman
Professor, Physics
& Electro-Optics



Christopher D. Brewer, Ph. D.
Committee Member
Technical Advisor
AFRL/RXPJE, WPAFB, OH



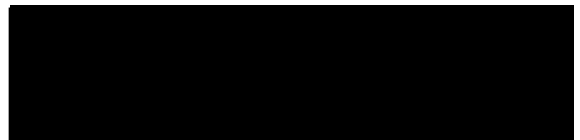
Joseph W. Haus, Ph. D.
Committee Member
Professor & Director,
Electro-Optics



Mark A. Walker, Ph. D.
Committee Member
Technical Advisor
AFRL/RXPJE, WPAFB, OH



Malcolm W. Daniels, Ph.D.
Associate Dean
School of Engineering



Joseph Saliba, Ph. D., P.E.
Dean, School of Engineering

ABSTRACT

NONLINEAR MATERIALS CHARACTERIZATION WITH FEMTOSECOND LASER PULSES

Name: Jenkins, Geoffrey D.
University of Dayton, May 2008

Advisor: Dr. Peter E. Powers

Laser-based applications in medical, scientific, communication, manufacturing, and defense industries all require the ability to predict phenomena resulting from interactions between the intense laser light and matter. Since the advent of mode-locked lasers, which can emit intense femtosecond-duration pulses, peak irradiances have reached astronomical values in table-top systems. This has greatly expanded the field of study for nonlinear laser-matter interactions. It is now possible to study dependencies of material properties on optical intensity, wavelength, pulse width, etc. Third order nonlinear optical (NLO) phenomena are currently of interest in much of this research, including NL absorption and refraction. NLO properties have been well-characterized for many 2nd order materials; however, there is a lack of data on 3rd order properties as well as a lack of efficient nonlinear media. The overall goal of this research was to implement and automate a fast system capable of measuring nonlinear absorption and refraction as ground work for NLO spectroscopy. A femtosecond laser source operating in the near infrared (775 nm) was used. The resulting system, using the z-scan technique, was employed in determining n_2 and/or β of previously undocumented optical media (RuPZn, RuPZnRu, PECVD Benzene, NS-86-3, NS-86-5, C-P5972). Excited state absorption studies were performed and saturated absorption was observed for selected media as well.

TABLE OF CONTENTS

ABSTRACT	iii
TABLE OF CONTENTS	iv
LIST OF FIGURES.....	vi
LIST OF TABLES	viii
CHAPTER 1 – Introduction.....	1
CHAPTER 2 – Nonlinear Absorption & Refraction.....	4
2.1 Nonlinear Refraction	5
2.2 Nonlinear Absorption.....	7
2.3 Frequency Dependence	9
2.4 Empirical Determination	11
CHAPTER 3 – The Z-Scan Measurement Technique	13
3.1 Open Aperture Z-Scan Theory.....	14
3.2 Closed Aperture Z-Scan Theory	17
3.3 Experimental Realization	20
3.3.1 Spatial Filter	21
3.3.2 Reference Detector	23
3.3.3 Pointing Stability.....	24
3.3.4 Aperture Size & Location	27
3.3.5 Calibration.....	29
3.3.6 Data Acquisition.....	31
3.3.7 Data Analysis	35
3.4 System Sensitivity & Error	37
CHAPTER 4 – NLO Study at 775 nm	41
4.1 Testing Reliability	41
4.2 Dyes and Solutions.....	44
4.2.1 AF455.....	44
4.2.2 Toluene.....	47

4.2.3 Carbon Disulfide	48
4.2.4 RuPZn.....	50
4.2.5 RuPZnRu.....	53
4.2.6 NS-86-3	55
4.2.7 NS-86-5	57
4.3 Thin Films	60
4.3.1 PECVD Benzene	60
4.3.2 Polyphenylene-Benzonitrile.....	62
4.4 Data Summary.....	65
CHAPTER 5 – Conclusions.....	66
Appendix A	70
REFERENCES.....	76

LIST OF ILLUSTRATIONS

Figure 2.1 – Self-phase modulation: self-lensing.....	6
Figure 2.2 – Two-photon absorption.....	8
Figure 2.3 – Linear vs. nonlinear absorption in an optical medium.....	9
Figure 2.4 – Behavior of $\chi^{(3)}$ near resonance.....	10
Figure 2.5 – Electronic transitions of 2PA and ESA.....	12
Figure 3.1 – Open aperture z-scan	14
Figure 3.2 – Open aperture z-scan transmittance.....	15
Figure 3.3 – Closed aperture z-scan.....	18
Figure 3.4 – Closed aperture z-scan transmittance.	19
Figure 3.5 – Z-scan implementation	20
Figure 3.6 – Spatial beam profile with and without spatial filter.....	22
Figure 3.7 – Elimination of noise from power fluctuations.	23
Figure 3.8 – Closed aperture z-scan data without use of reference detector.	24
Figure 3.9 – Exaggerated illustration of pointing stability.	25
Figure 3.10 – Pointing stability measurements with and without <i>Iris_I</i>	26
Figure 3.11 – Closed aperture baseline scan with and without <i>Iris_I</i>	27
Figure 3.12 – Relationship between sensitivity and aperture size for CA z-scans.	28
Figure 3.13 – Attenuator calibration.	29
Figure 3.14 – Relationship between V_{REF} and system energy.	30
Figure 3.15 – Relationship between V_{REF} and V_{SIG}	30
Figure 3.16 –Z-Scan protocol.	33
Figure 3.17 – Beam walking due to poor alignment.	34
Figure 3.18 – Equal but opposite beam walking due to sample alignment at focus.	34
Figure 3.19 – The x-axis shift correction for theoretical curve.	36
Figure 3.20 – Maximum detectable β .vs. I_0 for various sample thicknesses.....	37
Figure 3.21 – Maximum detectable n_2 .vs. I_0 for various sample thicknesses.	38
Figure 3.22 – Minimum detectable β vs. I_0 for various sample thicknesses.....	39

Figure 3.23 – Minimum detectable n_2 .vs. I_0 for various sample thicknesses.....	39
Figure 4.1 – CA z-scan data for SF11	43
Figure 4.2 – Molecular diagram of AF455	44
Figure 4.3 – OA z-scan data for AF455 (1)	45
Figure 4.4 – OA z-scan data for AF455 (2)	46
Figure 4.5 – OA z-scan data for AF455 (3).	46
Figure 4.6 – ESA relationship with I_0 for AF455	47
Figure 4.7 – Molecular diagram of Toluene	47
Figure 4.8 – Open and closed aperture z-scans of Toluene.	48
Figure 4.9 – Molecular diagram of CS ₂	48
Figure 4.10 – OA z-scan of CS ₂	49
Figure 4.11 – Open and closed aperture z-scans of CS ₂	50
Figure 4.12 – Molecular diagram of RuPZn	50
Figure 4.13 – Open and closed aperture z-scans of RuPZn	51
Figure 4.14 – OA z-scans of RuPZn for various I_0	52
Figure 4.15 – ESA vs. I_0 for RuPZn.....	53
Figure 4.16 – Molecular diagram of RuPZnRu.....	53
Figure 4.17 – OA z-scan data of RuPZnRu for various I_0	54
Figure 4.18 – Open and closed aperture z-scans if RuPZnRu.	55
Figure 4.19 – OA z-scan of NS-86-3	56
Figure 4.20 – Summary of NLA results for NS-86-3.	56
Figure 4.21 – Open and closed aperture data for NS-86-3.....	57
Figure 4.22 – The reduction of error from surface imperfections.....	58
Figure 4.23 – Summary of NLA results for NS-86-5	58
Figure 4.24 – Open and closed aperture data for NS-86-5.....	59
Figure 4.25 – Molecular diagram of Benzene.....	60
Figure 4.26 – The reduction of error from surface imperfections in a CA z-scan	61
Figure 4.27 – OA z-scan of all PP-BT films.....	62
Figure 4.28 – CA z-scan of the substrate, B270.....	63
Figure 4.29 – Example of negligible NLR effect of PP-BT films.	64
Figure 5.1 – Focal length of L_3 .vs. wavelength.....	68

LIST OF TABLES

Table 3.1 – Estimated error contributions.....	40
Table 4.1 – Comparison of data to previous results for n_2 reference media.....	44
Table 4.2 – Effective n_2 values from closed aperture z-scans.....	61
Table 4.3 – Isolated n_2 values from films and substrates.....	62
Table 4.4 – Summary of NLO data for various optical media.....	65

CHAPTER 1

Introduction

High power laser technology is rapidly advancing. In less than 50 years after their first successful demonstration, lasers have been shown capable of producing irradiances greater than that of all the sun's energy focused onto a pinhead [1], albeit for infinitesimal durations. This has become routinely possible with mode-locking, a method of operating a laser in which many longitudinal modes supported by both the laser cavity and gain medium share a fixed phase relationship and constructively interfere in a periodic manner to form intense pulses. The duration of each pulse is affected by the pulse shape, number of longitudinal modes supported by the gain medium, and the frequency spacing between those modes. Therefore, gain media with the largest bandwidths are capable of producing the shortest pulses. Titanium doped sapphire has a very large gain bandwidth (128 THz), is the most popular gain medium in ultrafast lasers, and is used in this research.

The term ultrafast generally refers to laser pulses with durations shorter than 10^{-12} seconds. Pulse widths from these lasers are approaching theoretical limits and durations shorter than 5 femtoseconds have been demonstrated in the infrared [1]. A motivation for the shortening of pulses is a large gain in peak optical power without having to increase energy. Another is the ability to study fast processes, such as chemical reactions at the atomic level. Scientists are hopeful that this will allow them to control such processes as

well [1]. Reducing energy requirements in this manner allows these lasers to be built in compact enclosures and increases affordability. As these high power lasers are becoming more common and integrated with industry, a lack of satisfactory optical media has become apparent and is limiting the development of certain technologies. For example, all-optical bistable devices [2], which form the basic building blocks of optical computing [3], are presently impractical due to a lack of efficient nonlinear media. Fast and reliable characterization systems are needed to aid chemists and physicists in the development of these materials for optical switching, telecommunications, multiphoton microfabrication, microscopy, and photodynamic therapy (PDT). The focus of this research is the development of such a system, which entails compromise between speed and accuracy as well as design considerations that allow for the accommodation of a wide range of experimental parameters such as wavelength, sample thickness, pulse width, etc.

This work pertains to the reaction between matter and intense optical radiation, which is the basis of nonlinear optics. The theory behind specific nonlinear phenomena is discussed in Chapter 2. This is complemented with analogies and applications. Chapter 3 contains theoretical and physical descriptions of the implemented measurement system (z-scan technique). The theoretical descriptions are separated by modes of operation, of which there are two (one each for determining n_2 and β). System optimization, both experimentally and analytically, is covered as well as data analysis and special considerations. Error is discussed as well. A compilation of NLA and NLR data taken from this system at 775 nm is found in Chapter 4. Included are reference and previously undocumented materials (NS-86-3, NS-86-5, RuPZn, RuPZnRu, C-P5972, PECVD Benzene, PP-Benzotrile) along with ESA studies in AF455, RuPZn, NS-86-3,

and NS-86-5. Concluding remarks are found in Chapter 5. Design and analysis considerations for broadband measurements are discussed as well as the practicality and feasibility of current and future measurement systems.

CHAPTER 2

Nonlinear Absorption and Refraction

For a long time, all optical media were thought to exhibit entirely linear behavior. When the invention of the laser enabled the study of materials at high optical intensities, it was found that certain properties were indeed intensity dependent. The nonlinear wave equation fully describes the properties of optical media in the relationship between the electric field vector, $E(\mathbf{r},t)$, and the polarization density vector, $P(\mathbf{r},t)$, and is expressed

$$\nabla^2 E - \frac{1}{c_0^2} \frac{\partial^2 E}{\partial t^2} = \mu_0 \frac{\partial^2 P}{\partial t^2} \quad (2.1)$$

where c_0 is the speed of light in a vacuum, t is time, and μ_0 is the permeability of a vacuum. It is common to see the polarization density expressed as a Taylor series given by [4]

$$P = \epsilon_0 (\chi E + \chi^{(2)} E^2 + \chi^{(3)} E^3 + \dots), \quad (2.2)$$

where ϵ_0 is the electric permittivity in a vacuum, χ is the electric susceptibility of the material, and the superscripts denote the orders of nonlinearity. The electric susceptibility is a measure of how easily a medium polarizes (induces or reorients dipoles) in response to an incident electric field and is related to the refractive index through the following expression:

$$n^2 = \frac{\epsilon}{\epsilon_0} = 1 + \chi \quad (2.3)$$

Several interesting phenomena occur when certain orders of nonlinearity are dominant in Equation 2.2. For example, when $\chi^{(2)}E^2$ is dominant, the material may be called a second order nonlinear medium. In this case, second-harmonic generation, optical rectification, the electro-optic effect, and three-wave mixing are possible [4]. If a medium is centrosymmetric, the second order nonlinearities will cancel and $\chi^{(3)}E^3$ will be dominant. A third order class of nonlinearities known as Kerr nonlinearities are of primary interest in this research.

2.1 Nonlinear Refraction

When a strong monochromatic electro-magnetic field is incident upon a Kerr medium, a nonlinear polarization is induced. This alters the effective refractive index to a degree linearly dependent on the intensity of the incident radiation [10]:

$$n = n_0 + n_2 I, \quad (2.4)$$

Equation 2.4 is called the Optical Kerr Effect and $n_2 \left(\frac{\text{m}^2}{\text{W}} \right)$ is known (for the scope of this work) as the coefficient of nonlinear refraction. This effect is usually caused by electronic polarization and is therefore essentially instantaneous, physically meaning that the radiation that induces these conditions is also affected by them. As a result, light can alter its own phase within a medium, which coupled with diffraction will cause it to change its spatial profile and refract. This is known as self-action and is utilized in the construction of several useful devices. In linear conditions (negligible contributions from $\chi^{2,3}$ in Eq. 2.2), refraction is governed by Snell's law [11]:

$$n_a \sin(\theta_a) = n_b \sin(\theta_b). \quad (2.5)$$

This is not sufficient to fully describe refraction if the amplitude of the incident electric field reaches a certain material dependent threshold. For a Kerr medium, the refractive index can spatially map the intensity profile of the incident radiation and result in a graded transverse index distribution. Since n_2 may be positive or negative, and the optical path length is defined as [12]

$$OPL = \int n(x, y, z) ds, \quad (2.6)$$

the most intense part of a laser pulse may “see” a larger or smaller path length than its edges, depending on the polarity of n_2 . Here $n(x, y, z)$ is the position dependent refractive index and $ds = \sqrt{dx^2 + dy^2 + dz^2}$ is the elementary arc length along the ray. Shown graphically in Figure 2.1 for a Gaussian pulse is a special case of self-action known as self-lensing. The lensing effect is caused by the deformation of phase fronts (red lines) as each region propagates a different optical path length and is delayed accordingly.

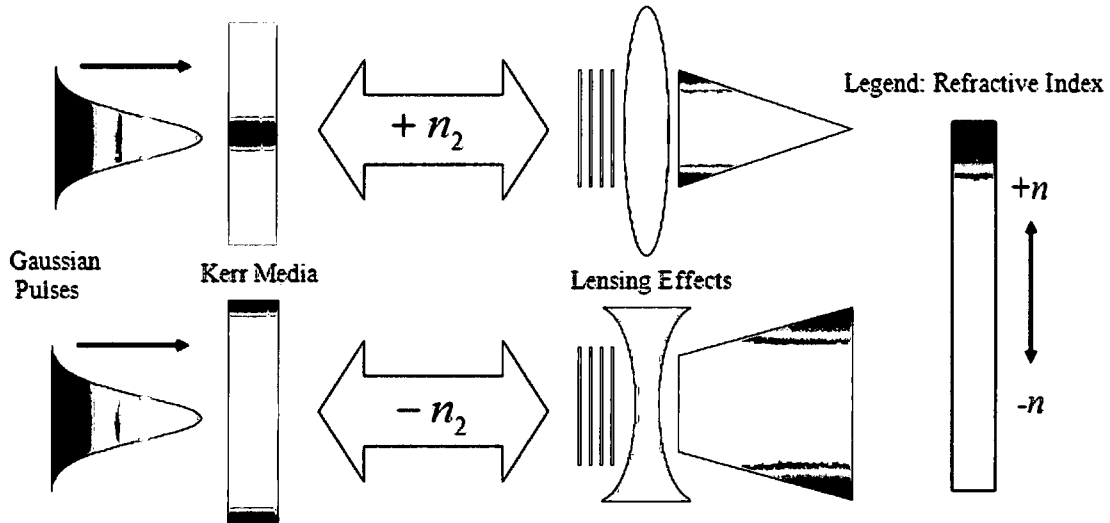


Figure 2.1 Self-phase modulation: self-lensing

Empirically determining n_2 proves to be a non-trivial endeavor because it has several major contributing factors that are highly dependent upon experimental conditions [5]:

$$n_2 = n_2(\text{electronic}) + n_2(\text{nuclear}) + n_2(\text{electrostrictive}) + n_2(\text{thermal}) \quad (2.7)$$

The electronic contribution is a product of the deformation of electron orbits and has a time scale given by an orbital period, which is less than an optical cycle in the VIS-NIR and thus is essentially instantaneous. Nuclear contributions arise from the translation or rotational motion of molecules and typically occur on a time scale > 500 fs, although some media, CS_2 for example, has a nearly instantaneous nuclear contribution. Electrostriction is the strain of the physical structure of a medium by an applied electric field. The thermal contribution is caused by excited electrons that relax to their previous orbits non-radiatively. These two contributions take effect on nanosecond and picosecond time scales, respectively.

2.2 Nonlinear Absorption

Media with third order nonlinearities may also exhibit nonlinear absorption, specifically two-photon absorption (TPA). This is a phenomenon in which two photons (not necessarily of the same frequency) combine to bridge the energy gap of a medium that is larger than the individual energies of the photons as shown in Figure .2.

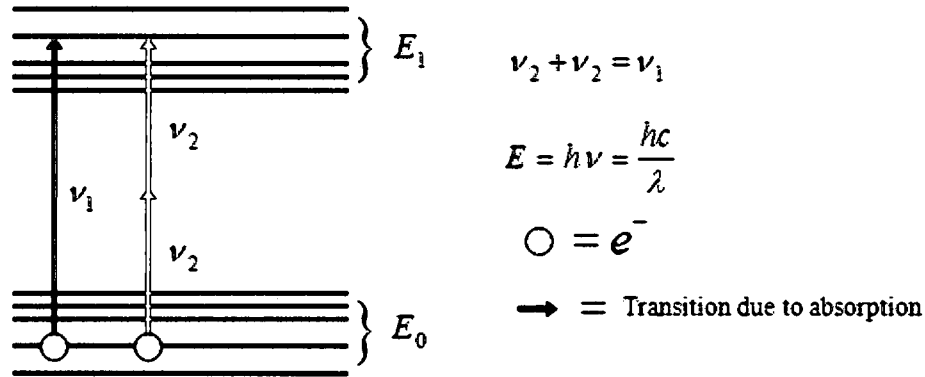


Figure 2.2 - Two-photon absorption

Here ν is the optical frequency, $\frac{\omega}{2\pi} = \frac{c}{\lambda}$, E is the bandgap energy of the medium in electron volts (eV); h is Planck's constant, equivalent to 6.626×10^{-34} (J · s), and the yellow circles represent electrons. Since these photons must coincide in both space and time, the rate of TPA increases with intensity and the overall absorption increases through [10]

$$\alpha(I) = \alpha + \beta I, \quad (2.8)$$

where α is the linear absorption coefficient (m^{-1}) and β is the two-photon absorption coefficient ($\frac{\text{m}}{\text{W}}$). In the linear regime, Beer's law Eq. 2.9 is commonly used to relate input (I_0) and transmitted (I) intensities to the thickness (t) and absorption properties (α) of a medium:

$$I = I_0 e^{-\alpha t} \quad (2.9)$$

In the presence of two-photon absorption, the intensity transmission becomes [6]:

$$I = \frac{I_0}{1 + \beta I_0 t} \quad (2.10)$$

The difference between linear and nonlinear absorptive properties of an optical medium is shown graphically in Figure 2.3 for arbitrary constants using the equations above.

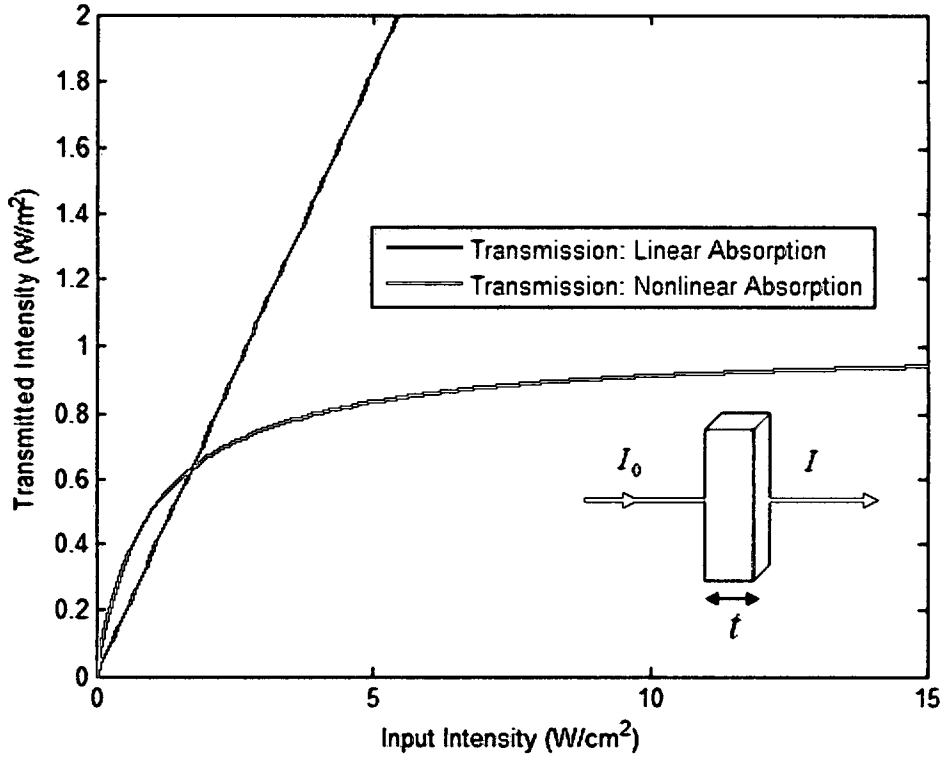


Figure 2.3 Linear vs. nonlinear absorption in an optical medium

Nonlinear refraction always accompanies nonlinear absorption; however, the reverse is not true. CaF_2 , for example, has an n_2 of $(2.77 \times 10^{-7} \frac{\text{cm}^2}{\text{GW}})$ and a negligible value for β , as seen by a wavelength of 775 nm [7]. The coupling between these coefficients will be discussed in a following section.

2.3 Frequency Dependence of NLA and NLR

NLA and NLR are dispersive properties, meaning their values vary as a function of optical frequency, or wavelength. The $\chi^{(n)}$ susceptibility is composed of a sum of real and imaginary parts which correspond to refraction and absorption, respectively [8]:

$$\chi^{(n)} = \chi_{Re}^{(n)} + i\chi_{Im}^{(n)} \quad (2.11)$$

For a given third order susceptibility the NLA and NLR coefficients may be found from

$$\beta = \frac{\chi_{Im}^{(3)} \omega}{n_0^2 \epsilon_0 c^2} \quad (2.12)$$

$$n_2 = \frac{\chi_{Re}^{(3)}}{2n_0^2 \epsilon_0 c} \quad (2.13)$$

Absorption and refraction are coupled through the Kramers-Kronig relations, in which their relationship is defined for all frequencies, ω [8]:

$$n_2(\omega) = \frac{c}{\pi} \int_0^\infty \frac{\beta(\omega')}{\omega'^2 - \omega^2} d\omega' \quad (2.14)$$

Many optical media contain multiple resonant frequencies where the real and imaginary parts of the susceptibility reach local maxima or minima. The behavior of the real and imaginary components of the susceptibility near a resonant frequency of a medium is displayed in Figure 2.4.

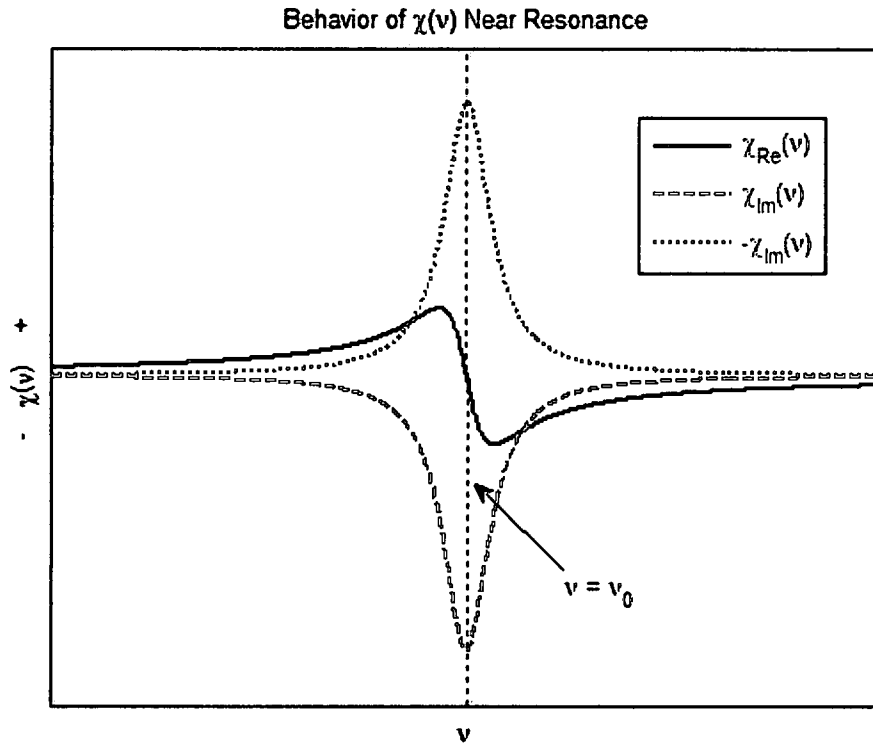


Figure 2.4 Behavior of $\chi(\nu)$ near resonance

They are governed by the following approximations [9], where $\nu = \frac{\omega}{2\pi}$; ν_0 is the resonant frequency, and $\Delta\nu$ is the FWHM of $\chi_{Im}(\nu)$:

$$\chi_{Im} = -\chi_0 \frac{\nu_0 \Delta\nu}{4} \frac{1}{(\nu_0 - \nu)^2 + (\Delta\nu/2)^2} \quad (2.15)$$

$$\chi_{Re} = 2 \frac{(\nu - \nu_0)}{\Delta\nu} \chi_{Im}(\nu) \quad (2.16)$$

As is indicative of the broken red line, a negative value for the imaginary susceptibility represents gain rather than absorption, as certain media exhibit; however, this is not observed in this work. Broadband material characterization has become an important tool in finding these resonances, especially in the nonlinear regime where there is a significant lack of data. This research is ground work for the implementation of a broadband measurement system. Although broadband data was not acquired in this work, this system was designed to function with a wavelength range of 775 nm – 2 μ m.

2.4 Empirically Determining NLA and NLR

The focus of this work is the implementation of a system capable of measuring n_2 and β . A mode-locked Ti:Sapphire laser emitting a wavelength of 775 nm is used and emits 175 femtosecond pulses at a repetition rate of 500 Hz. In determining n_2 , it is assumed that the main contribution is electronic because these pulses are short relative to the reaction times of the other contributions. There may be other phenomena present that can affect NLA and NLR in addition to those already mentioned. Excited state absorption (ESA) and saturated absorption, for example, may be experimentally perceived as third order nonlinearities. Figure 2.5 is a comparison of TPA and ESA. Unlike TPA, where two photons combine to excite an electron over a relatively large energy band gap, ESA occurs when two consecutive linear absorptions are made and is

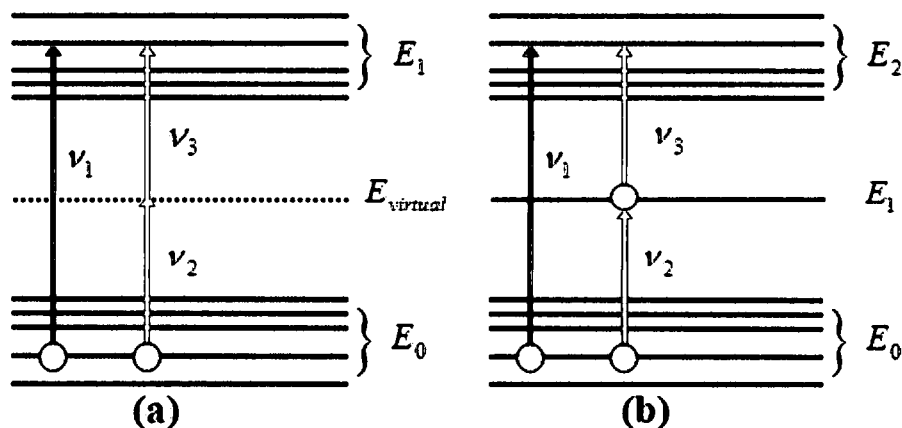


Figure 2.5 (a) electronic transitions of TPA, (b) electronic transitions of ESA

possible by the presence of an intermediate 1PA resonance. This intermediate resonance may be an inherent property of a medium or impurities within. As these electronic transitions occur on the order of 1 fs, ESA is entirely possible with the pulse widths used in this work. Saturated absorption is also considered, where the ground state (E_0 in Figure 2.5) becomes fully depleted of electrons at increased irradiances. In this case there are no electrons available to absorb incident photons, and an overall reduction in absorption becomes apparent. This is demonstrated in the data section. It is impossible for any single experiment to isolate and absolutely determine the individual contributions to these nonlinear processes, therefore the NLA and NLR coefficients determined in this work are “effective” values, not attributed to be the results of any single mechanism.

CHAPTER 3

The Z-Scan Measurement Technique

In 1989, Mansoor Sheik-Bahae *et al.* [10] introduced a new method for measuring the nonlinear refractive index and absorptive properties of optical media called the z-scan technique. This method was highly sensitive and required the use of only one laser beam, making it far simpler than other methods such as nearly degenerate three-wave mixing [13], degenerate four-wave mixing [14], and nonlinear interferometry [15]. It has become quite a common tool in the optics community and its results are well accepted. Many improvements and variations of this method have been published by researchers from around the world [16-35].

The fundamental operation of this method relies on transmission measurements of a sample as it is translated through the focus of a laser beam. This increases the irradiance on the sample while keeping the beams properties unaltered. The z-scan technique effectively converts phase distortions to amplitude modulation as seen in transmission measurements made through a finite, or closed, aperture in the far field. Properties of nonlinear refraction are determined from the analysis of these phase distortions. When transmission measurements are made through an open aperture, where all light passed through the sample is detected, nonlinear absorption may be determined. The theory behind these two modes of operation is presented in the following sections.

3.1 Open Aperture Z-Scan Theory

An open aperture z-scan provides nonlinear absorption information of sample media. Open refers to the mode where all light transmitted through a sample is captured by a signal detector in the far field. For this discussion the detector is considered to be in the far field at a distance d if it is much larger than the Rayleigh range of the beam, that is if [10]

$$d \gg z_0 = \frac{\pi \omega_0^2}{\lambda} \quad (3.1)$$

The transmission is monitored while a sample is translated through the focus of the beam as shown in Figure 3.1.

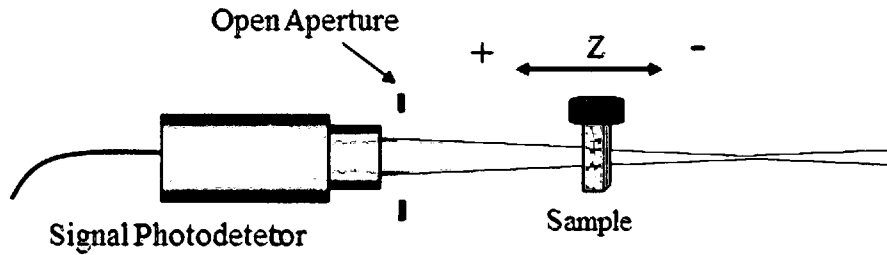


Figure 3.1 Open aperture z-scan

The incident on-axis irradiance becomes a function of z and may be calculated through

$$I(z) = \frac{2 \cdot \ln[1 + \sqrt{2}] \cdot E}{\pi \cdot \tau \cdot w_x(z) \cdot w_y(z)} \quad (3.2)$$

where E is the beam energy in Joules, τ is the pulse width in seconds, and $w_{x,y}$ are the beam radii in the x and y dimensions, respectively, at a propagated distance z . As the irradiance increases rapidly near focus, the presence of TPA becomes apparent via decreased transmission. Since the spatial profile of the beam is symmetric about focus, the irradiance decreases at the same rate after focus and results in increased transmission as the rate of TPA decreases. Shown in Figure 3.2 are theoretical transmittance trends

characteristic of an open aperture z-scan for various values of q_0 , a parameter directly proportional to the incident irradiance upon the sample, defined as $q_0(z, t) = \frac{\beta I_0(t) L_{\text{eff}}}{1 + z^2/z_0^2}$.

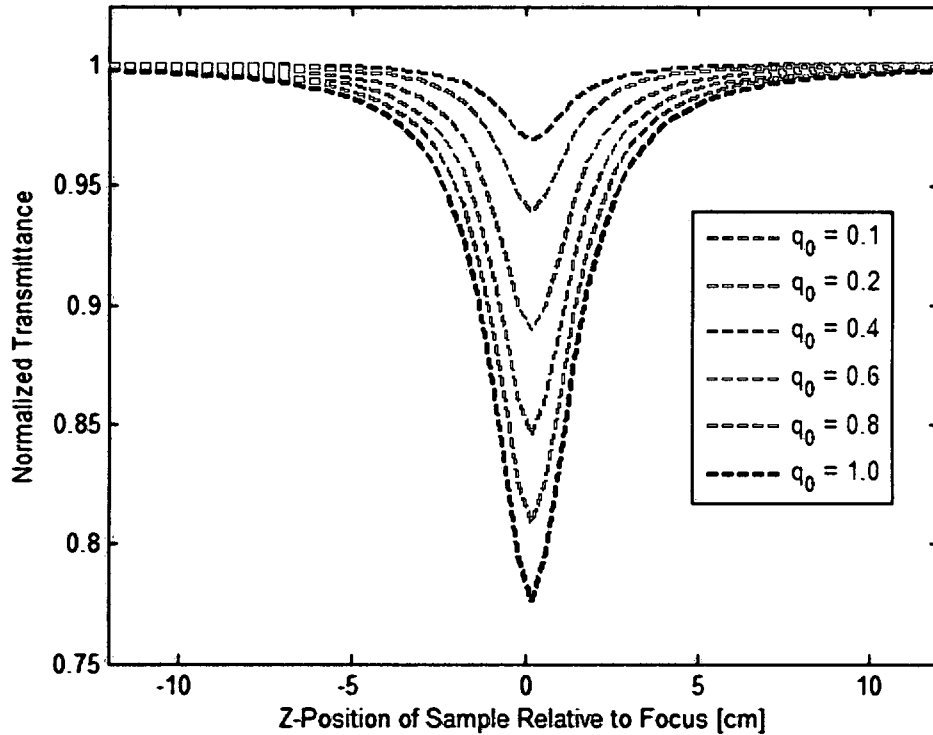


Figure 3.2 Open aperture z-scan transmittance

This is mathematically modeled as follows, assuming a TEM_{00} Gaussian beam of the form [10]

$$E(r, z, t) = E_0(t) \frac{w_0}{w(z)} e^{\left(\frac{-r^2}{w^2(z)} - \frac{ikr^2}{2R(z)} \right)} e^{-i\varphi(z, t)} \quad (3.3)$$

where $w(z)$ and w_0 are the beam radii at z and focus, respectively; k is the free space wave vector given by $k = \frac{2\pi}{\lambda}$; $R(z)$ is the radius of curvature of the wavefront at z ; $E_0(t)$ contains temporal information of the pulse and the electric field amplitude at focus, and $e^{-i\varphi(z, t)}$ contains radially uniform phase variations. When the slowly varying envelope approximation (SVEA) is applied and a “thin” sample is assumed, the relationship between intensity and absorption becomes [10]

$$\frac{dl}{dz'} = -\alpha l - \beta l^2 \quad (3.4)$$

where z' is the propagation distance of the beam in the sample. It has been empirically determined by Bahae *et al.* [10] that this condition is met if the sample thickness is smaller than the Rayleigh range of the beam, z_0 . The irradiance at the exit surface of the sample may be expressed [10]

$$I_e(z, r, t) = \frac{I(z, r, t)e^{-\alpha L}}{1 + q(z, r, t)} \quad (3.5)$$

where $q(z, r, t) = \beta I(z, r, t)L_{\text{eff}}$. It is important to realize that L_{eff} is the effective length of a sample medium and is a function of linear absorption and physical length [10]:

$$L_{\text{eff}} = \frac{1 - e^{-\alpha L}}{\alpha} \quad (3.6)$$

When the irradiance function is spatially integrated over r , the power (P) transmitted to the detector becomes a function of time and sample position [10]:

$$P(z, t) = \int_0^r \frac{I(z, r, t)e^{-\alpha L}}{1 + q(z, r, t)} dr = \frac{\pi w_0^2 I_0(t)}{2} e^{-\alpha L} \left[\frac{\ln[1 + q_0(z, t)]}{q_0(z, t)} \right] \quad (3.7)$$

Temporally integrating the power function yields the normalized energy transmittance as would be seen by a detector, here assuming a Gaussian temporal profile [10]:

$$T(z) = \frac{1}{\sqrt{\pi} q_0(z, 0)} \int_{-\infty}^{\infty} \ln[1 + q_0(z, 0)e^{-\tau^2}] d\tau \quad (3.8)$$

This transmittance function is numerically fit to open aperture z-scan data to extract β . It is beneficial to keep $|q_0| < 1$, as this simplifies the analysis for closed aperture z-scans used for determining n_2 . This condition can be satisfied by reducing the irradiance incident upon the sample. It can be deduced from Figure 3.2 that the irradiance should be attenuated such that the minimum transmission does not drop much further below 80%. This allows for the beam to be mathematically propagated using a binomial series

expansion in powers of q , necessary for modeling the electric field at the aperture in closed aperture z-scans. β , however, may be determined for any q by evaluating Eq. 3.8.

3.2 Closed Aperture Z-Scan Theory

A closed aperture z-scan operates in the same manner as the open aperture z-scan, but with a finite aperture placed in front of the detector in the far field. The light transmitted through a sample is baffled by this aperture such that the linear transmittance is [10]

$$S = 1 - e^{(-2r_a^2/w_a^2)} \quad (3.9)$$

where r_a and w_a denote the radii of the aperture and the beam at the aperture, respectively. S is unity for open aperture z-scans described in the previous section, where r_a is infinite. This is the mechanism that converts the z-scan into a phase-amplitude transducer. As a sample medium is scanned along z , self-lensing is induced near focus and the cone of light that reaches the detector in the far field is altered, thereby increasing or decreasing the amount of light that passes through the aperture. If n_2 of a sample medium is negative it will form a negative lens with an irradiance-dependent focal length. As NLR is induced before focus it will have a collimating effect on the beam and more light will be transmitted through the aperture, resulting in a peak in transmission. A lens positioned at the focus of a beam has little to no effect, therefore the transmission returns to the linear baseline at focus. As the sample passes focus, the symmetric spatial beam profile creates the same lensing effect as before focus, but results in a transmission minimum because the negative lensing further diverges the already diverging beam. Far from focus, both before and after, the incident irradiance is insufficient to induce NLR

and the measured transmission becomes constant. This scenario is demonstrated in Figure 3.3. If n_2 is positive, the minimum and maximum transmissions will occur before and after focus, respectively, opposite to the case for negative n_2 .

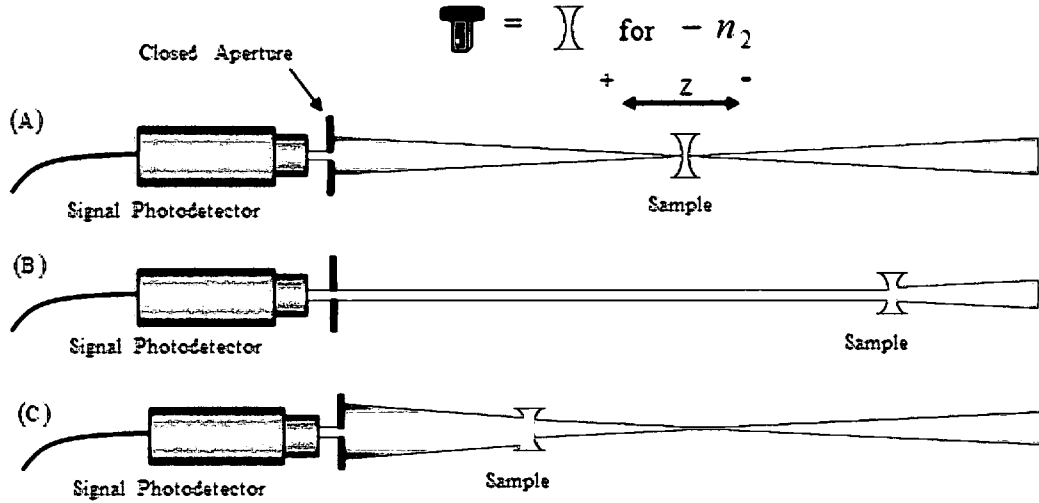


Figure 3.3 Closed Aperture Z-Scan: (a) a lens at focus has little to no effect on beam propagation; (b) a negative lens collimates a converging beam, increasing optical throughput to the detector; (c) a negative lens diverges a diverging beam, decreasing optical throughput to the detector

The theoretical description of the transmittance is found using the same analysis used in obtaining Eq. 3.4. Applying the SVEA and assuming a “thin” sample, the change in phase is found to be related to the incident intensity through [10]

$$\frac{d\Delta\varphi}{dz'} = \Delta n(I)k \quad (3.10)$$

When negligible NLA is assumed, Eq. 3.10 can be solved to find $\Delta\varphi$ at the back surface of the sample [10]:

$$\Delta\varphi_e(z, r, t) = \frac{\Delta\Phi_0(t)}{1 + z^2/z_0^2} e^{\left(\frac{-2r^2}{w^2(z)}\right)} \quad (3.11)$$

where $\Delta\Phi_0(t) = k\Delta I_0(t)n_2L_{\text{eff}}$ is the on-axis phase shift at focus. This intensity dependent phase distortion is incorporated into the electric field at the exit surface (E_e) of

the sample and must be propagated to the far field to obtain the electric field at the aperture (E_a). As the detector will only see what is transmitted through the aperture, E_a must be radially integrated to the size of the aperture. The transmitted power becomes [10]

$$P(\Delta\Phi_0(t)) = c\epsilon_0 n_0 \pi \int_0^{r_a} |E_a(r, t)|^2 r dr, \quad (3.12)$$

The normalized transmittance function provided below [10] yields a peak-valley or valley-peak curve asymmetric about focus as shown in Figure 3.4.

$$T(z) = \frac{\int_{-\infty}^{\infty} P(\Delta\Phi_0(t)) dt}{S \int_{-\infty}^{\infty} (I_0(t) \pi w_0^2 / 2) dt} \quad (3.13)$$

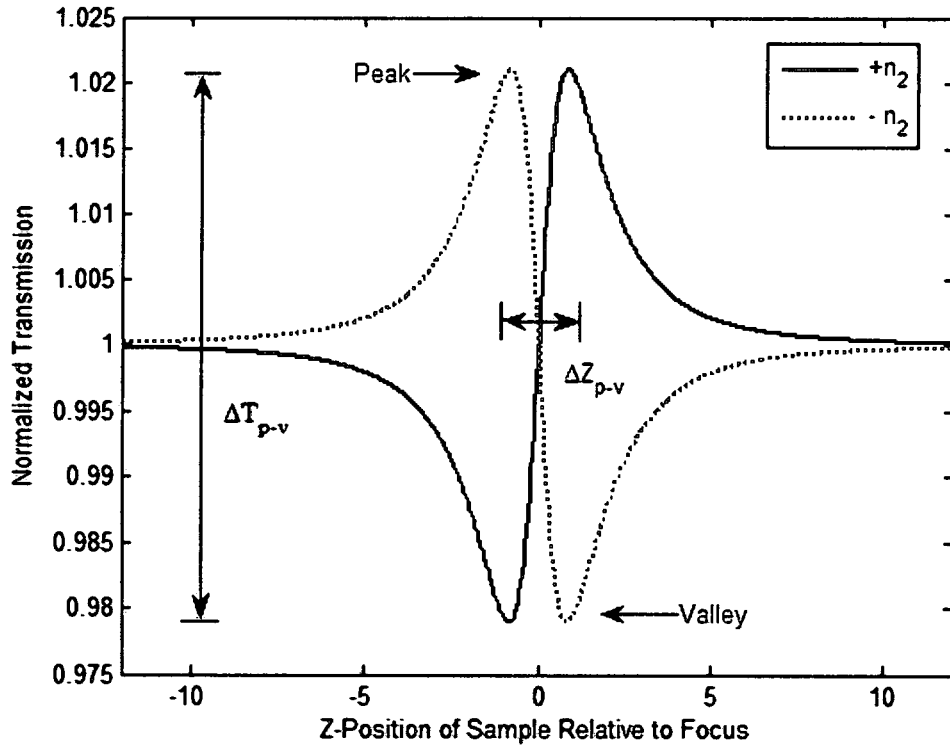


Figure 3.4 Closed aperture z-scan transmittance

If the peak appears before focus ($-z$), n_2 is negative and vice versa. S is related to the sensitivity of closed aperture z-scans and should be kept small in order to maximize the peak-valley separation, ΔT_{p-v} . This separation is linearly dependent upon $\Delta\Phi_0$ and is in

fact the only value needed to accurately estimate n_2 . Sheik Bahae *et al.* have numerically determined that, to within 2% accuracy, n_2 may be determined from the following equation, so long as $|\Delta\Phi_0| \leq \pi$ [10]:

$$n_2 \cong \frac{\Delta T_{p-v}}{0.406(1-S)^{0.25} k I_0(t) L_{eff}} \quad (3.14)$$

For third order NLR, the peak and valley of the transmittance curve are separated approximately by $\Delta Z_{p-v} \cong 1.7z_0$ [10]. If this is not found to be true empirically, $\chi^{(3)}$ is not the sole contributor to NLR. If $\chi^{(5)}$ becomes significant, for example, ΔZ_{p-v} will decrease approximately to $1.2z_0$. If the separation becomes larger, the “thin” sample approximation may be violated. Further discussion of these issues is conducted by Chapple *et al.* [36].

3.3 Experimental Realization

Shown in Figure 3.5 is an implementation of a z-scan measurement system designed to meet the approximations mentioned above. The detectors are made of

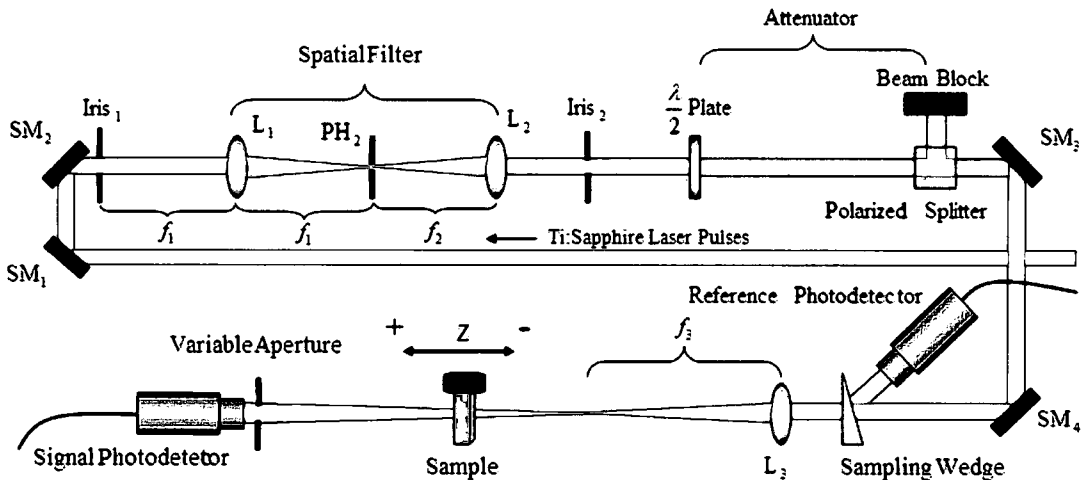


Figure 3.5 Z-Scan implementation

Germanium and are responsive from $\lambda = 0.6 - 2\mu\text{m}$. Silver mirrors (SM) were chosen for their high reflectance over a broad range of wavelengths, and L_3 was chosen such that a sample could be translated ± 10 times the Rayleigh range without exceeding the physical limits of the translation stage, measured to have a range of ± 43 cm from the desired focal plane of the beam. The maximum spot size that satisfies this condition was deduced by setting the Rayleigh range to 4.3 cm:

$$w_{0,\text{max}} = \sqrt{\frac{z_R \lambda}{\pi}} = \sqrt{\frac{(4.3\text{cm})(775\text{nm})}{\pi}} \cong 103\mu\text{m} \quad (3.15)$$

Considering the “thin” sample approximation, where the Rayleigh range must be larger than the thickness of a sample, a minimum spot size of $26\mu\text{m}$ was calculated assuming the largest sample to be tested would be 3 mm. In finding an appropriate focal length to achieve a focus of this region, the beam diameter at the lens had to be known. This was measured to be approximately 4 mm with a CCD camera, in both x and y dimensions. Therefore the focal length was chosen to be 500 mm, as specified at 532 nm. Accounting for dispersion with Sellmeier coefficients for BK7 [42], the focal length of the lens at 775 nm was 506 mm, resulting in a spot size of approximately $60\mu\text{m}$.

3.3.1 Spatial Filter

Due to the necessity of a high quality Gaussian beam profile for accuracy, a spatial filter was employed to reduce noise riding on the beam. This was accomplished by choosing L_1 to be 300 mm, which focused the noisy beam to a spot size of just under $50\mu\text{m}$, and choosing PH_2 to be $50\mu\text{m}$. L_2 was chosen to be 250 mm and collimated the beam to approximately 4 mm in diameter. A CCD camera was scanned along the focus of the beam and its profile was fitted to a Gaussian function to determine its divergence relative to an ideal Gaussian beam. M^2 values of 1.15 and 1.05 were calculated for the x

and y dimensions of the beam, respectively, after implementing the spatial filter. An M^2 value is a quality factor used to describe the rate at which a laser beam diverges relative to that of an ideal Gaussian beam. A perfect Gaussian beam will have M^2 values of unity in both x and y dimensions. In this work, since M_x^2 is larger than M_y^2 , the spatial profile of the beam increased more rapidly in width (x) than it did in height (y) through propagation. Shown in Figure 3.6 is a comparison of spatial profiles of the beam at focus with and without the spatial filter. Notice Figure 3.6 (a) is ovular while Figure 3.6 (b) is circular and therefore more ideal.

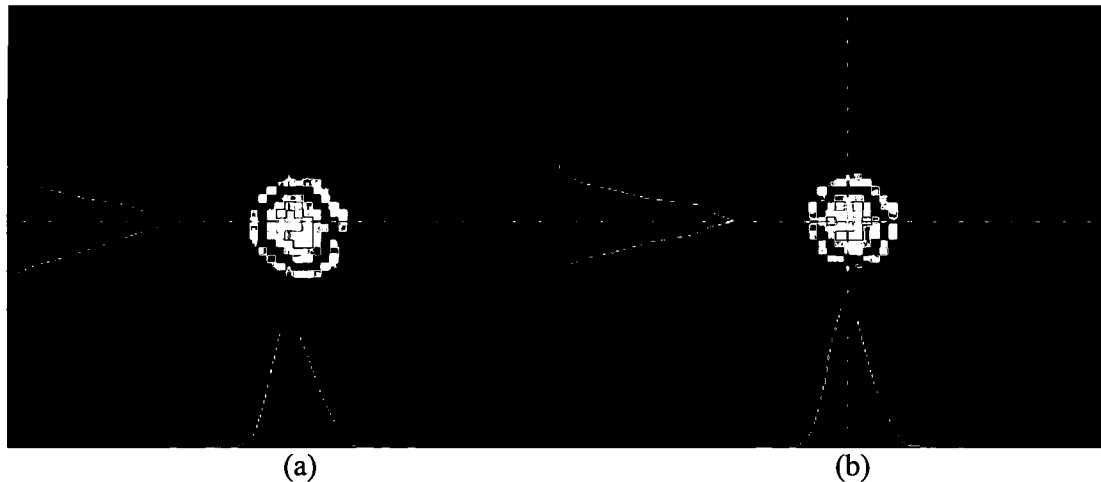


Figure 3.6 – Spatial beam profile at focus (a) without spatial filter, and (b) with spatial filter

Chapple *et al.* [36] investigated the effects of beam quality on z -scan accuracy by comparing ΔT_{p-v} values as obtained with an ideal Gaussian beam to those obtained with beams of decreased quality. In order to achieve 5% accuracy, it was concluded that M^2 values of less than 1.1 and 1.3 are needed for closed and open aperture z -scans, respectively. Hermann [19], Mian [17], and Zhao *et al.* [37] have introduced analyses for z -scans with non-Gaussian beams; however they are complex and unnecessary if a beam can be sufficiently forced to be Gaussian, as done here.

3.3.2 Reference Detector

A reference detector was used to reduce noise caused by random pulse to pulse power fluctuations inherent to the operation of the laser. The sampling wedge served to send a small fraction of the beam to this detector while only causing a slight lateral shift of the beam to the signal detector, which was accounted for during alignment. When the voltage from the signal detector was divided over that of the reference detector, pulse to pulse readings became significantly more constant. Figure 3.7 shows the elimination of this noise from data taken in an open aperture z-scan without a sample medium.

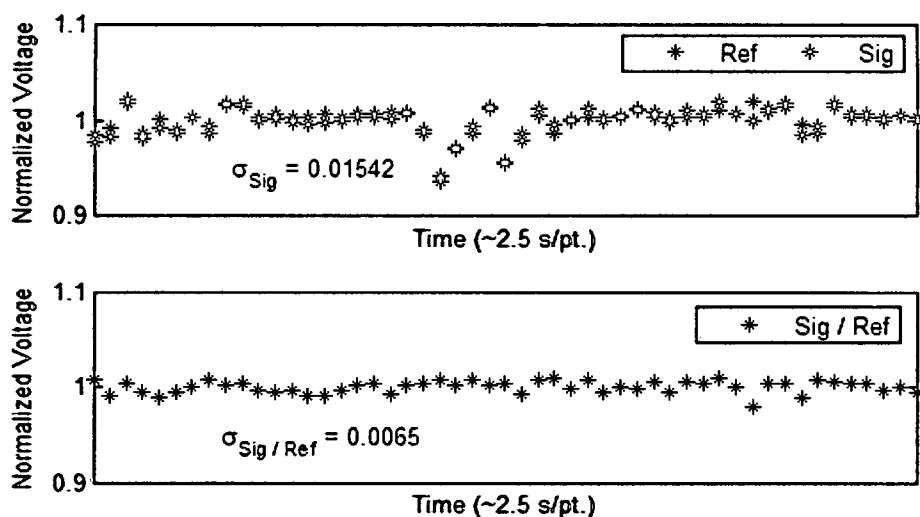


Figure 3.7 – Elimination of noise from power fluctuations

As is apparent in the figure above, the noise was greatly reduced by using a reference detector. The standard deviation from the ideal value of unity was reduced by over 200%. In Figure 3.8, closed aperture z-scan data are shown both with and without the use of a reference detector and illustrates why the removal of this noise is beneficial.

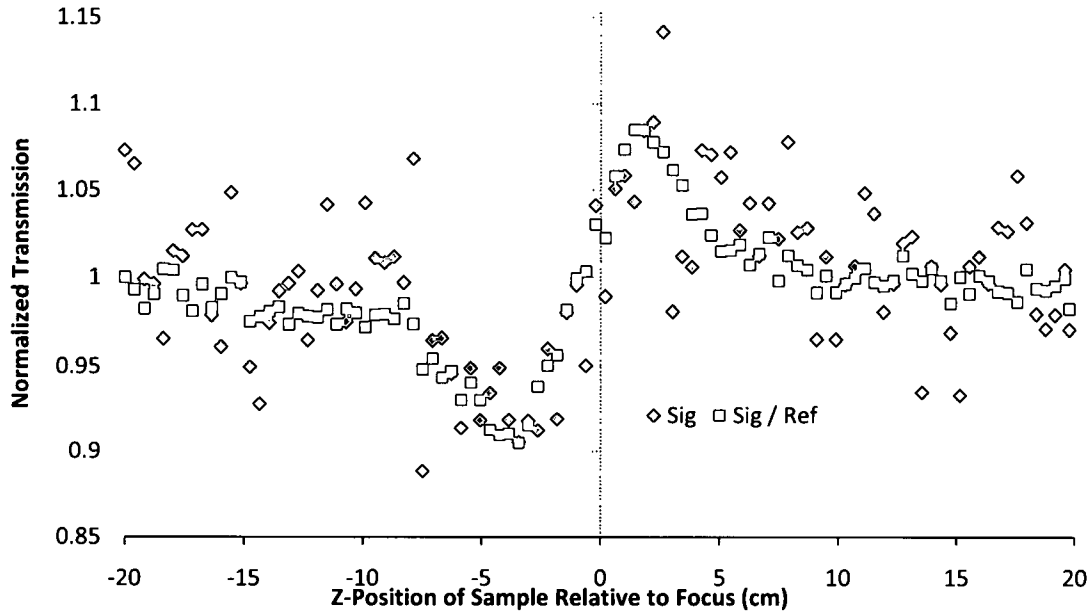


Figure 3.8 – Closed aperture z-scan data with and without use of a reference detector

The peak-valley difference (ΔT_{p-v}) for the two plots above differ by approximately 34%. Because n_2 is linearly dependent upon this value as demonstrated in Eq. 3.14, this would contribute 34% error to this NLR measurement.

3.3.3 Pointing Stability

The laser beam exhibited noticeable “jitter,” a common characteristic of laser operation. The peak location of the Gaussian shaped beam varied randomly from pulse to pulse within a small area. This can add error to measurements, specifically closed aperture z-scans, because some pulses may be baffled by the aperture in such a way as to be interpreted as radiation-matter reactions within the sample. An illustration of a stray pulse in a closed aperture z-scan is shown in Figure 3.9.

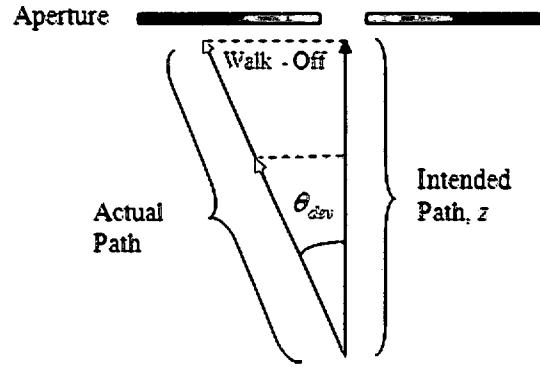


Figure 3.9 – Exaggerated illustration of pointing stability

This error can be reduced somewhat through averaging and moving the experiment as close to the laser as possible. In this work, the laser was approximately four meters from the signal detector in terms of optical path length. The walk-off shown above is a function of the propagated distance of the beam, where θ_{dev} , is random:

$$Walk - Off = Z \times \tan(\theta_{dev}) \quad (3.16)$$

In an attempt to further reduce the effect of pointing stability, $Iris_1$ was placed one focal length in front of the spatial filter lens, L_3 (see Figure 3.5). Since L_1 serves to Fourier transform the beam as seen one focal length before it, it was thought that closing $Iris_1$ around the edges of the beam at this location would result in a more stable energy throughput because the energy is more “flat” near the peak of the Gaussian beam. Diffraction effects were not characterized, however the location of the pinhole and the collimating lens were adjusted until maximum transmission and collimation were achieved, respectively. The pointing stability was measured with a Cohu 4812 CCD camera and Spiricon LBA710PC software for 3000 shots both before and after $Iris_1$ was introduced. This measured the location of the beam’s centroid and provided standard deviation data. Results are shown in Figure 3.10.

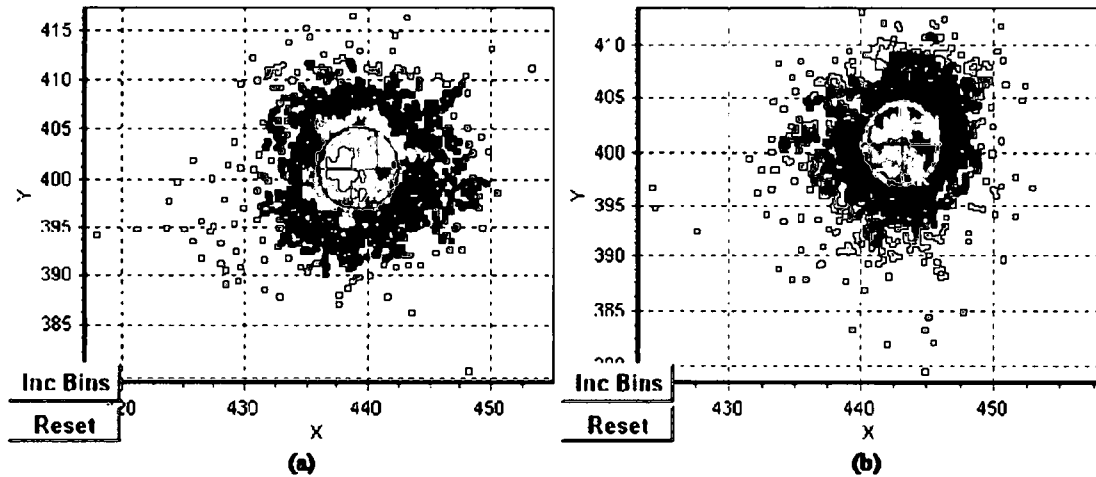


Figure 3.10 – Pointing stability measurements (a) without $Iris_I$, and (b) with $Iris_I$

The introduction of $Iris_I$ reduced the standard deviation of the centroid locations by 18.53% and 7.2% in the x and y dimensions, respectively. Standard deviation (σ) is a measure of the spread of values of a random variable (transmission in this case) about its mean, and is given by [43]

$$\sigma = \sqrt{\frac{1}{N} \sum_{i=1}^N (x_i - \bar{x})^2} \quad (3.17)$$

where N is the number of data points, x_i is data point i , and \bar{x} is the mean of all data points. Baseline z-scans were performed with and without $Iris_I$ as well, that is, z-scans without a sample that should ideally result in constant transmission. These were performed frequently and always after a change was made to the experiment to measure noise. Results are shown in Figure 3.11 for a closed aperture z-scan. The standard deviation was reduced by 81.8% by $Iris_I$ in this case.

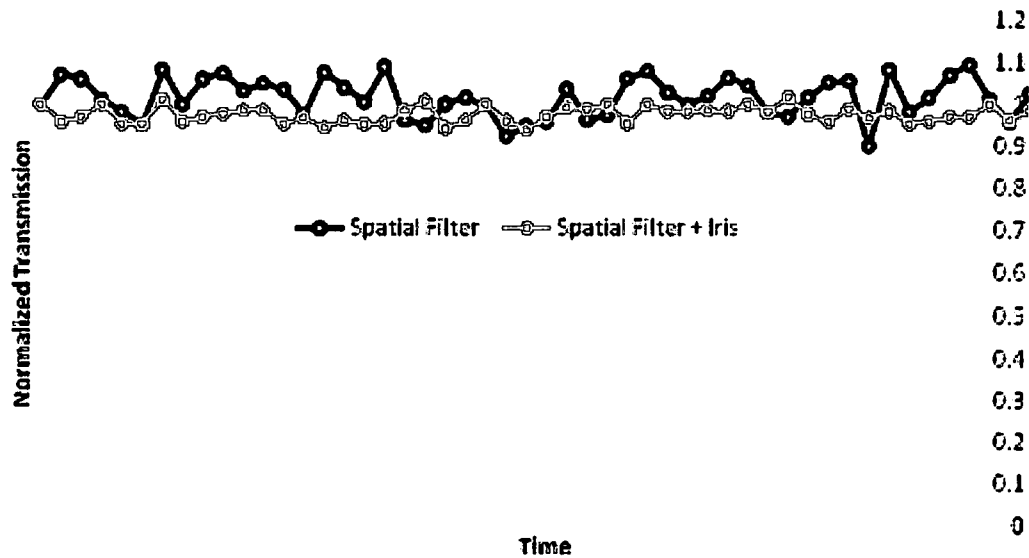


Figure 3.11 – Closed aperture baseline scan with and without *Iris*,

3.3.4 Aperture Size & Location

The sensitivity of closed aperture z-scans to NLR is at a maximum when the aperture size is at a minimum. Experimentally, there may be a need for compromise between aperture size and detector sensitivity. If S becomes too small, the voltage generated from incident photons on the signal detector may not be distinguishable from the inherent electronic noise of the signal detector's circuitry.

The variable aperture in Figure 3.5 had a minimum diameter of 0.75 mm as was measured with digital calipers sensitive to 0.01 mm. Due to the large magnitude of irradiances needed to induce optical nonlinearities in sample media, this aperture size was not problematic and the signal had to be attenuated to prevent damage to the detector. An empirical study of the relationship between aperture size and ΔT_{p-v} was performed on a 3 mm thick sample of BK7 glass for a constant irradiance in a closed aperture z-scan. The results are shown in Figure 3.12 below. This shows that ΔT_{p-v} is largest for the smallest

aperture size and separates the peak and valley of the transmission curve furthest from the noise floor.

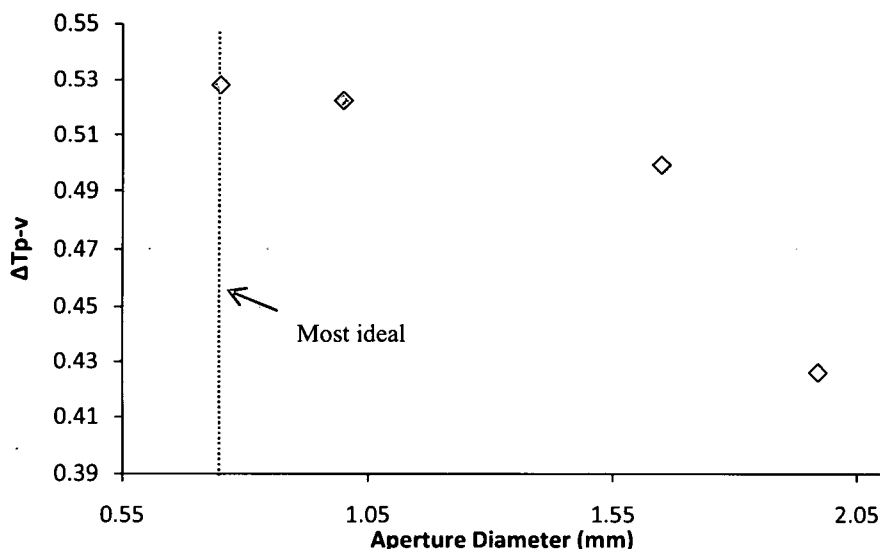


Figure 3.12 – Relationship between sensitivity and aperture size for a closed aperture z-scan

To validate the closed aperture z-scan equations, the aperture must be placed in the far field, which was defined above. Ideally, this distance would be infinite, however a general rule of thumb of ten Rayleigh ranges from focus has been established and results in ΔT_{p-v} values that are within 1% of those that would be obtained at infinity [36]. At first, the aperture was placed at the maximum distance from focus that was possible with available lab space, but this became a problem with open aperture z-scans. As the beam diverged while propagating this distance, it became larger than the active surface of the detector ($\sim 1 \text{ cm}^2$) and the data began show a peak and valley as if an aperture were present. The problem was resolved by moving the aperture closer to focus, to distance of approximately 34 cm. This was found to be sufficient to accommodate both closed and open aperture z-scans, as a Rayleigh range of 1.46 cm was measured for this system. A corrected value for ΔT_{p-v} of [36]

$$\frac{\Delta T_{p-v}(z_1)}{\Delta T_{p-v}(\infty)} = 1 + \frac{0.9}{0.8 + (z_1/z_R)^2} = 1.0017, \quad (3.18)$$

was neglected. Here z_1 is the distance between focus and the aperture.

3.3.5 Calibration

In order to acquire meaningful data, it was essential to know the response of the detectors to both a range of optical energies and to each other. National Instruments' LabVIEW software was utilized to automate several calibration routines. The first tested Malus' Law (Figure 3.13) on a pyroelectric energy meter and generated a look-up table defining the relationship between the wave-plate angle of the attenuator and optical

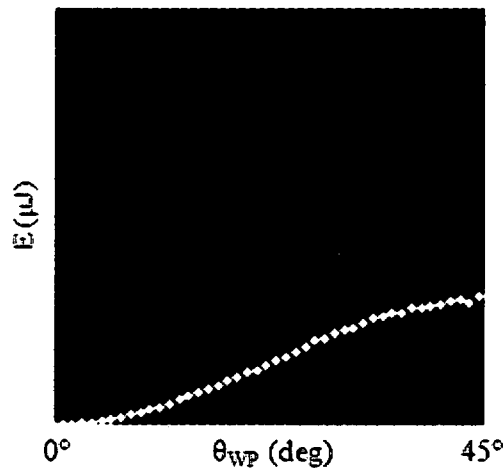


Figure 3.13 – Attenuator Calibration

energy. This was essential for automating the control of energy throughput to the signal detector as well as determining the maximum and minimum energies available to the system. Typically, the energy measurements from 30 pulses were averaged for wave-plate angle increments of 0.5 degrees. Next, the voltage of the reference detector (V_{Ref}) was monitored as the attenuator altered energy throughput by interpolating values in the

aforementioned E- θ look-up table. As desired, the relationship between V_{Ref} and system energy proved to be linear over the entire range. This is shown in Figure 3.14.

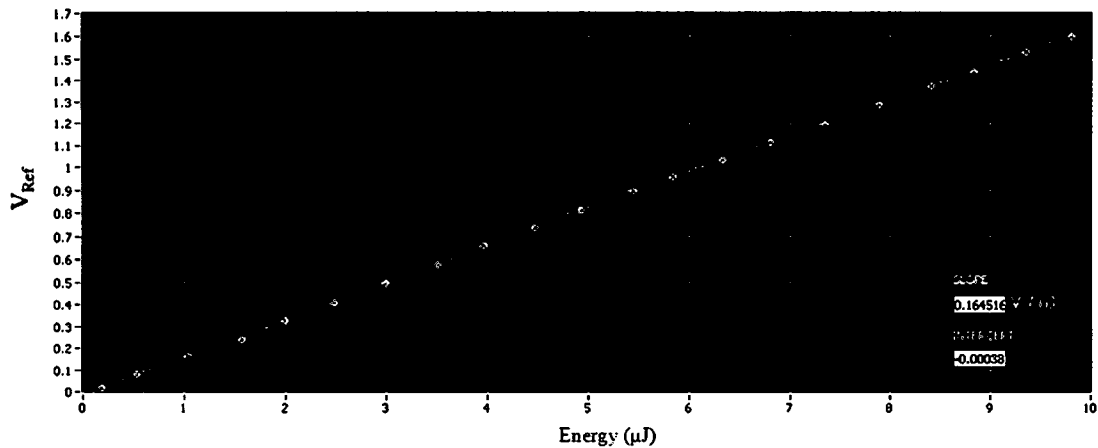


Figure 3.14 – Relationship between V_{Ref} and system energy

Although the signal and reference detectors were of the same make and model, their response relative to each other needed to be known because they were attenuated differently. The reference detector saw a small fraction of what the signal detector saw and therefore required less attenuation. This may reverse in the case of a closed aperture z-scan, for which a separate calibration is needed while the aperture is closed. The relationship between V_{Ref} and V_{Sig} proved to be linear as well, where differences in attenuation and aperture size affected the slope. See Figure 3.15.

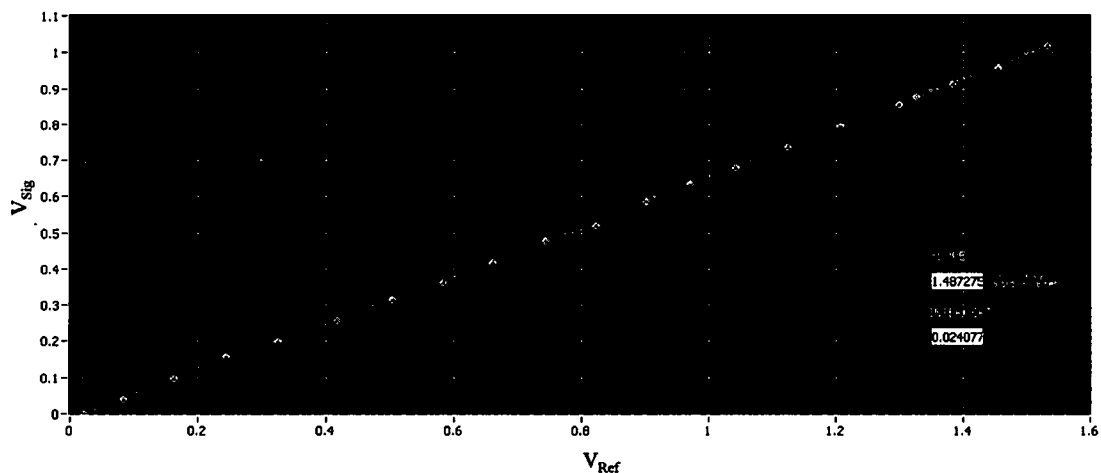


Figure 3.15 – Relationship between V_{Ref} and V_{Sig}

Because these relationships were linear, the conversion of the detector voltages to energies was possible through the multiplication of a constant. For example, V_{Ref} can be converted to energy by multiplying by the inverse of the slope from Figure 3.14:

$$E_{\text{Ref}} = V_{\text{Ref}} \times \left(\frac{V_{\text{Ref}}}{\mu\text{J}} \right)^{-1} \quad (3.19)$$

Similarly, V_{Sig} may be converted to energy through the following operation, using the slope from Figure 3.15:

$$E_{\text{Sig}} = E_{\text{Ref}} \times \left(\frac{V_{\text{Sig}}}{V_{\text{Ref}}} \right)^{-1} \quad (3.20)$$

Since the z-scan theory has been derived for normalized transmission data, the conversion from voltage to energy had no effect and was not necessary in most cases. It can be beneficial when comparing data from media with significant differences in linear absorption, however. The specified energies for z-scans are defined from within the media, and variations in linear absorption may require irradiance adjustments in analysis.

3.3.6 Data Acquisition & Protocol

LabVIEW software was also utilized to acquire and manipulate data as well as automate the measurement processes. A program was written to control the linear translation motor, the wave-plate rotational motor, and oscilloscope. A Tektronix TDS7404 oscilloscope captured signals from both the signal and reference detectors and was triggered by a fast photodiode that was able to detect the leakage behind a mirror. It was also used to capture data from the energy meter for when used for calibration. An acquisition mode called “fast-frame” was used to capture 100 pulses for both detectors at each z-position of the sample. The pulse to pulse power fluctuations were eliminated as

described above and this information was averaged before being stored in a spreadsheet file for post-experiment analysis. The average of 100 pulses was retained and stored for each detector as well for manipulation if the need for energy conversion became apparent. The ratio of V_{Sig} and V_{Ref} was normalized to its first value, where $z \gg z_0$. This value is representative of the “baseline,” where transmission is constant and no significant nonlinear effects are present.

This program allowed great flexibility for z-scan measurements, as the user was able to specify many experimental parameters, including:

- Starting position of sample relative to focus
- Ending position of sample relative to focus
- # z-positions to acquire data
- Translation motor speed
- Energy input
- # Pulses to acquire per z-position
- Beam waist at focus, w_{0x} and w_{0y}
- Wavelength, λ
- Beam diameter (x and y dimensions) at L_3
- M_x^2 and M_y^2
- Sample thickness, L

Although not all of these parameters were necessary in conducting z-scan data acquisition, they were stored with the data and greatly simplified the data analysis. A block diagram illustrating the protocol of a z-scan measurement is shown in Figure 3.16.

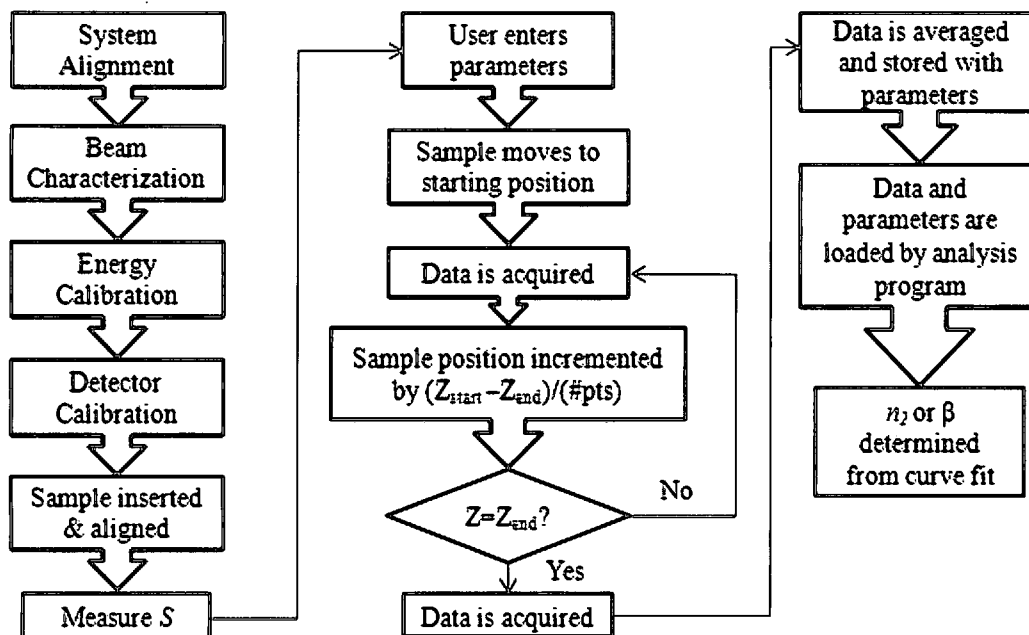


Figure 3.16 – Z-scan protocol

System alignment was critical, especially for closed aperture z-scans, where it was imperative that the beam be centered on the opening of the aperture. This was accomplished by removing L_3 and iteratively adjusting SM_3 and SM_4 until maximum transmission was obtained through multiple irises temporarily placed between the sampling wedge and the signal detector. With this done, L_3 was reinserted and adjusted in x and y dimensions until the reading from the apertured signal detector was maximized. This provided excellent results and was performed frequently.

Samples were placed in a vice mounted on the translation stage. In order to minimize beam “walking” from a wedged sample, samples were moved to focus and rotated until the Fresnel reflections returned to their origin near the center of L_3 . The need for flat media has been one of the major criticisms of the z-scan method. The walking effect and its mitigation are displayed in Figures 3.17 and 3.18 for a closed aperture z-scan of CS_2 and an open aperture z-scan of AF455, respectively.

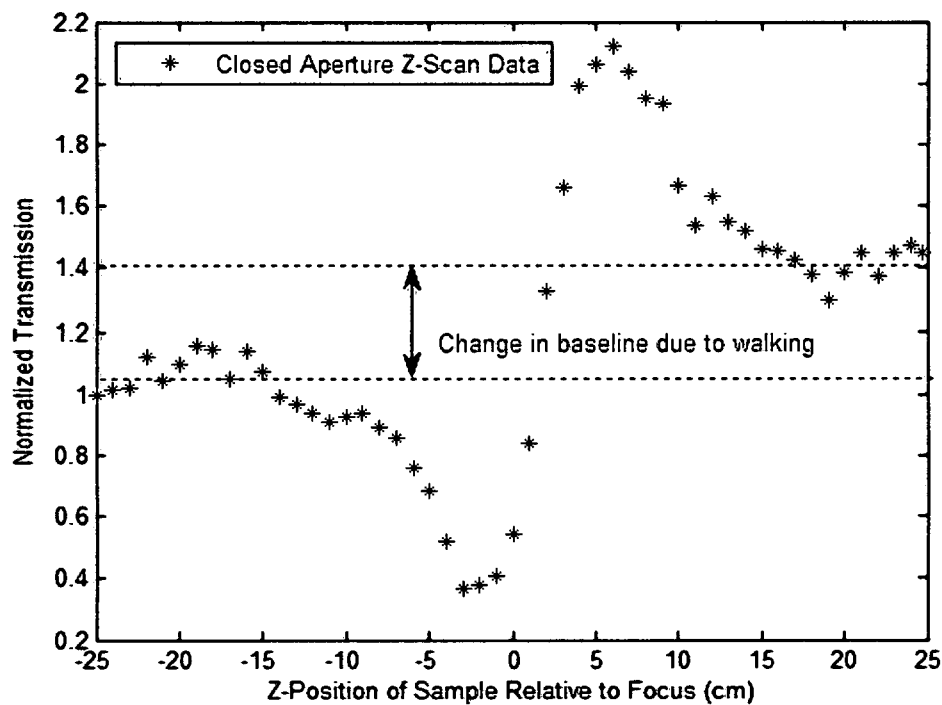


Figure 3.17 – Beam walking due to poor alignment

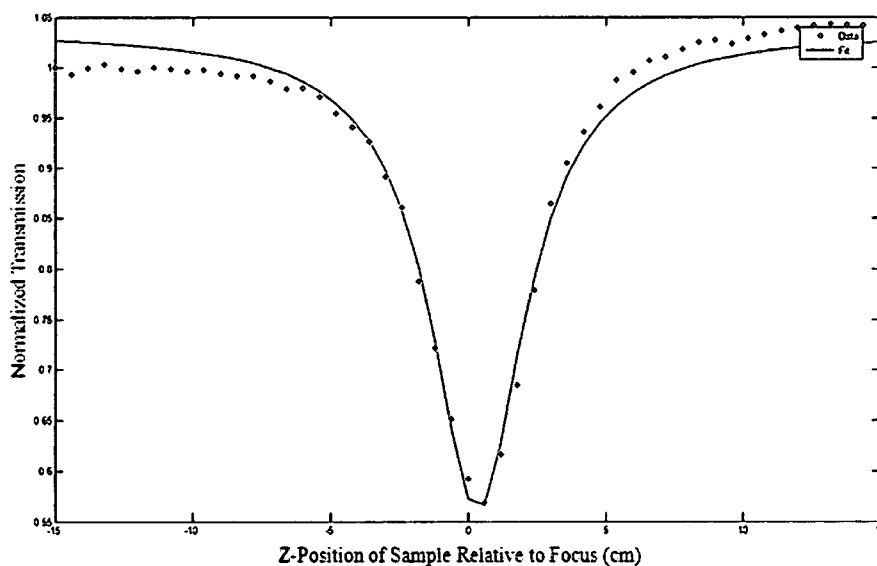


Figure 3.18 – Equal but opposite beam walking due to sample alignment at focus. The green line represents a theoretical fit of the data and is affected little by walking.

The linear transmission of the aperture, S , is a quantity easily measured. While the sample is in place at a distance $z \gg z_0$, V_{Sig} is recorded while the aperture is open and again when it is closed. S can then be calculated from

$$S = \frac{V_{Sig}(r_a \neq \infty)}{V_{Sig}(r_a = \infty)} \quad (3.21)$$

and resulted in typical values of approximately 0.1 for the minimum aperture size mentioned previously. It is important to take this measurement with the sample medium in place because losses due to Fresnel reflections and linear absorption will cancel in the ratio.

3.3.7 Data Analysis

As indicated in the protocol flowchart, data and experiment parameters are loaded by a data analysis program. Two curve fitting analysis programs were written in Matlab; one each for closed and open aperture z -scans. The code for these programs can be found in Appendix A. Both programs utilize the function *fminsearch*, which finds a minimum of a multi-variable function starting at user defined initial guesses for each variable. This has been referred to as “unconstrained nonlinear optimization” [38]. The function fed into *fminsearch* created an artificial data set with the initial variable guesses plugged into the theoretical equation of interest and performed a sum of least squares with the experimental data. The variables were changed until *fminsearch* converged to a solution, for up to 50,000 iterations. Three variables were used for both closed and open aperture analyses. These include n_2 or β and an x and y offset. These offsets proved to be very convenient. The y offset helps compensate for a change in the baseline and is noticeable in Figure 3.18, where the green fitted line begins and terminates at a value greater than unity. The x offset allows the user to set the “home” of translation stage at a rough

estimate of the focal plane's location, eliminating the need for the time consuming task of manually finding the exact location of the focal plane with a CCD camera. This is demonstrated in Figure 3.19 for an open aperture z-scan of AF455.

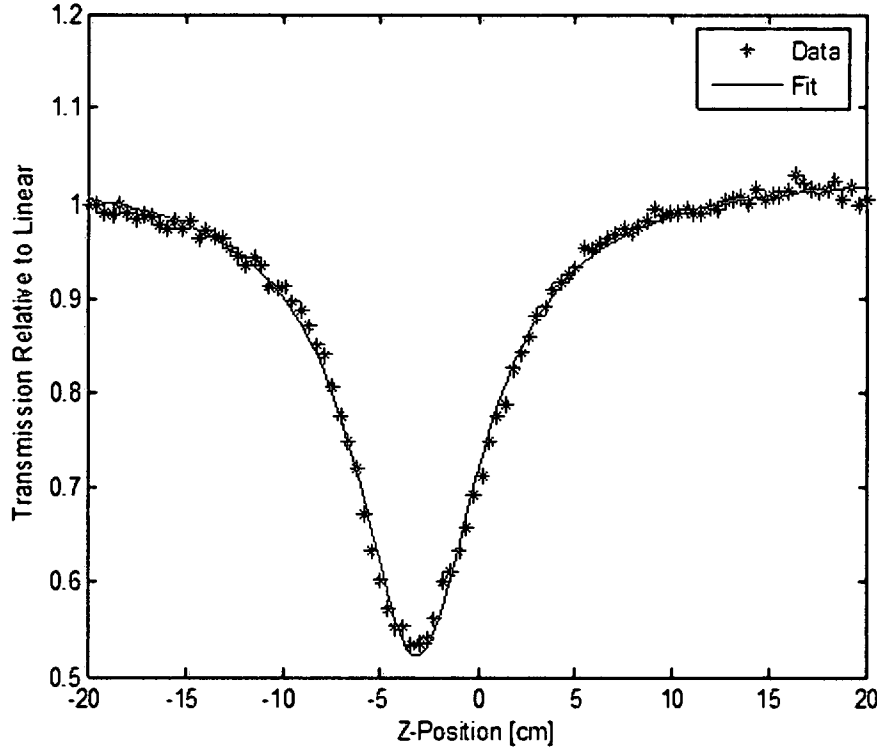


Figure 3.19 – The x-axis shift correction for theoretical curve

For open aperture analyses, Eq. 3.8 is fit to data. Although only ΔT_{p-v} is required to estimate n_2 , curve fits were performed on closed aperture data as well, using the normalized transmission function as derived by Sheng-Li Guo *et al.* [16]:

$$T(x) = 1 + \frac{(1-S)^\mu \sin \xi}{S(1+x^2)} \Delta \Phi_0 \quad (3.22)$$

$$\mu = \frac{2(x^2 + 3)}{x^2 + 9} \quad (3.23)$$

$$\xi = -\frac{4x \ln(1-S)}{x^2 + 9} \quad (3.24)$$

$$x = z/z_0 \quad (3.25)$$

3.4 System Sensitivity & Error

With the focused spot size of $60\text{ }\mu\text{m}$ produced by L_3 , a 175 fs pulse width, and a range of available energies of $0.1\text{-}10\text{ }\mu\text{J}$, the peak irradiance available to the sample arm of this system ranged from approximately $9\text{-}900\text{ }\frac{\text{GW}}{\text{cm}^2}$. The minimum irradiance in this range is due to the non-ideal extinction ratio of the attenuator. This can be reduced further by manually adding neutral density (ND) filters in the beam path. The maximum detectable NLR and NLA coefficients were determined (Figures 3.20-21) for several sample thicknesses by setting $q_0 = 1$ and $\Delta\Phi_0 = \pi$. These are the maximum values that keep the accuracy of the theory within 10%. Thicknesses chosen are typical values for solids and films and meet the thin sample approximation for this system.

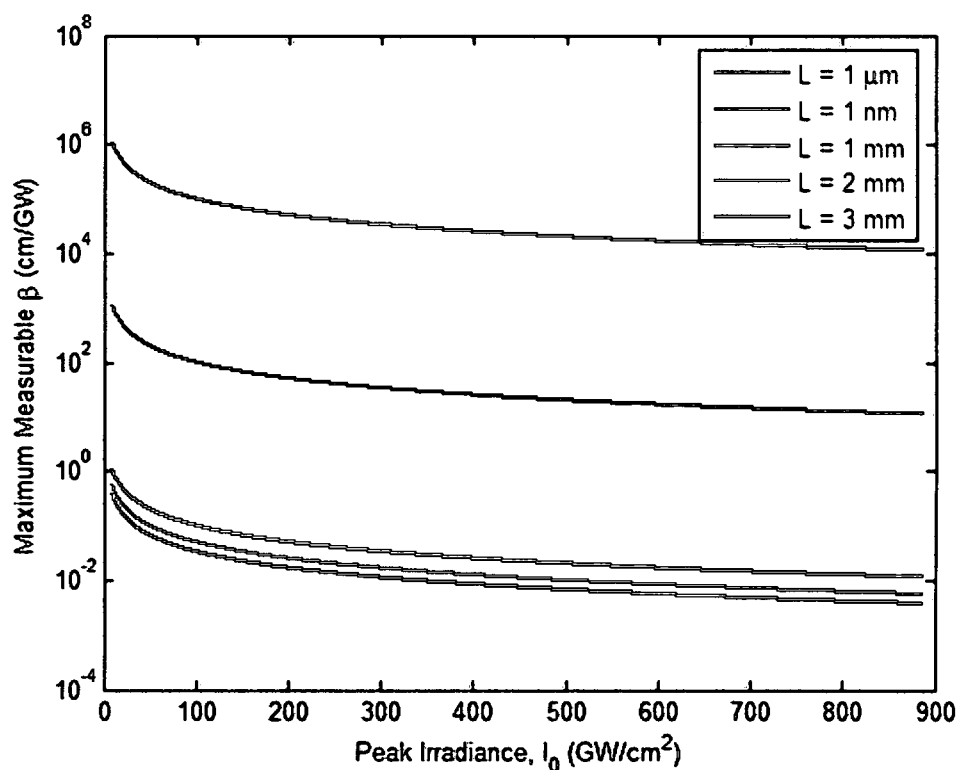


Figure 3.20 – Maximum detectable β vs. peak irradiance for various sample thicknesses

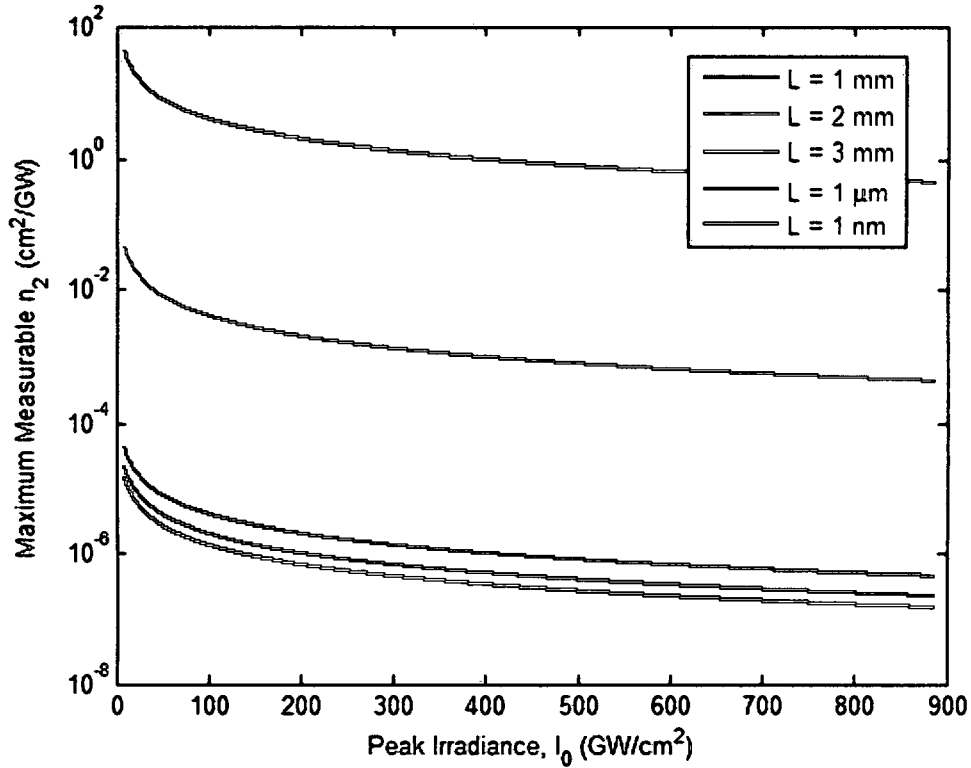


Figure 3.21 – Maximum detectable n_2 vs. peak irradiance for various sample thicknesses

The minimum detectable NLR and NLA coefficients are determined by the noise of the system as measured via baseline scans (Figure 3.11). For example, if the transmission dip due to NLA in an open aperture z-scan is within the standard deviation of the baseline scan data, it will not be measurable. Plotted in Figure 3.22 and Figure 3.23 are the approximate minimum detectable NLA and NLR coefficients, using the baseline scan data shown in Figure 3.11. The noise around the ideal baseline is approximately ± 0.05 and it is assume a signal-to-noise ratio of 2 is detectable, that is, a signal that strays from the baseline twice as far as the noise. This corresponds to a minimum q_0 of $\cong 0.4$ for an open aperture z-scan, referring to Figure 3.2. For a closed aperture z-scan, this corresponds to a minimum detectable ΔT_{p-v} value of approximately 0.2.

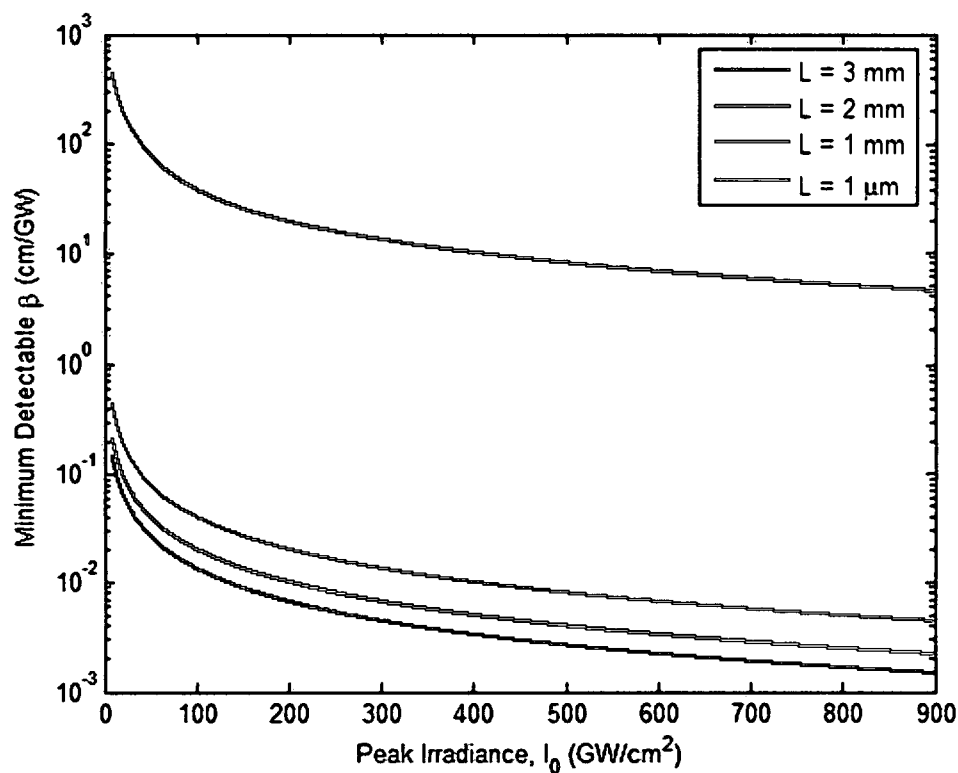


Figure 3.22 – Minimum detectable β vs. peak irradiance for various sample thicknesses

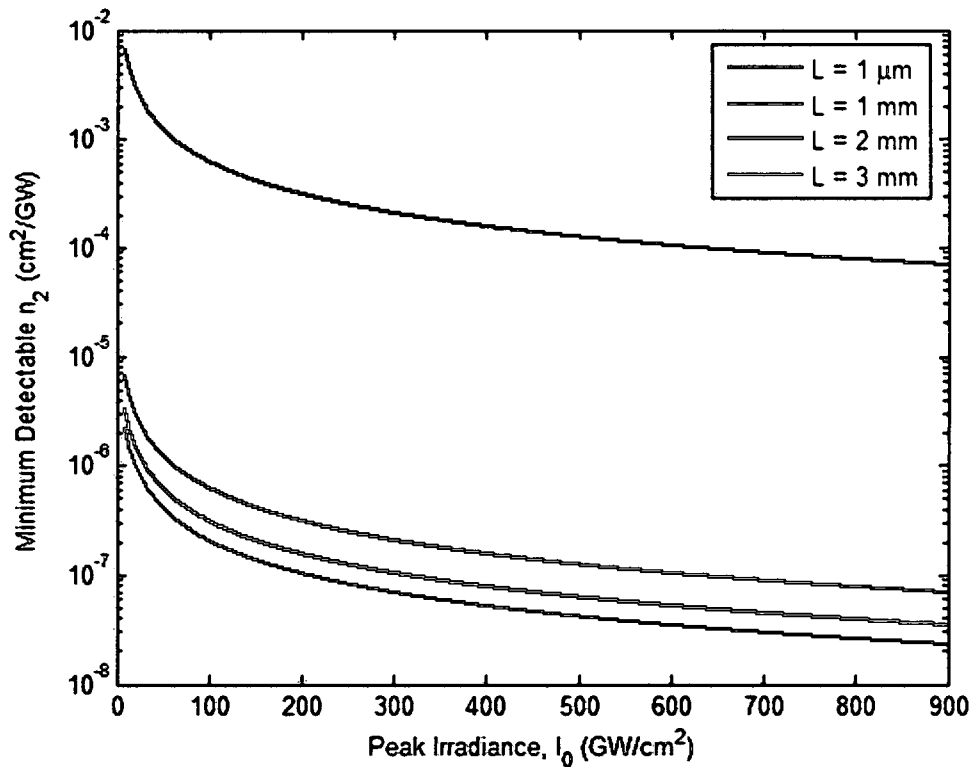


Figure 3.23 – Minimum detectable n_2 vs. peak irradiance for various sample thicknesses

The main sources of error for measurements by this system are the absolute energy measurement by the pyroelectric joule-meter, the pulse width measurements from the auto-correlator, and spot size measurements by the CCD camera. Estimated error contributions are displayed in Table 3.1. These are typical values in literature, as these error sources are largely unavoidable.

Table 3.1 – Estimated error contributions

<i>Parameter</i>	<i>Device</i>	<i>Make</i>	<i>Model</i>	<i>Error</i>
Temporal Pulse Width	Auto-correlator	Clark-MXR	AC-150	~6%
Beam Waist	CCD Camera	Cohu	4812	~10%
Energy	Pyroelectric Joule-Meter	Molelectron	J3-09	~5%
Theory	Eq. (3.14) & Eq. (3.18)	[10] & [16]	-	~10%
Total	-	-	-	~30%

CHAPTER 4

NLO Study at 775 nm

Several previously undocumented nonlinear optical (NLO) properties of materials were measured using the z-scan measurement system. The scanned materials include thin films, solutions, and glasses. The form of optical media has application dependent benefits. For example, if an anti-reflection coating is needed for a lens, it is more practical to deposit a thin, solid film over its surface rather than submerge it in a solution. For this reason it is of particular interest to know if a given material retains its optical properties as its state of matter is changed, for example, from a liquid to a solid film. Z-scans are capable of measuring all forms of optical media, provided that samples are of high quality. Films that are unevenly distributed across a substrate may provide erroneous data as the beam may see different parts of a medium through translation. Error due to poor sample quality can be reduced to a limited extent and is examined on a case to case basis in the following study.

4.1 Testing Reliability

In order to trust measurements from any experiment, it is wise to measure a well characterized "reference" material to see if the results match those that are widely trusted. Finding an appropriate reference value can be a daunting task because NLO properties are very sensitive to parameters such as pulse width, irradiance, and wavelength. Values

yielded from z-scan analyses may be considered absolute if the system is trusted and proven to replicate established measurements. If this is not the case, closed aperture z-scan measurements may be analyzed in reference to a well characterized material by performing z-scans on both the reference material and material of interest and applying Eq. 4.1 [39]. This also allows closed aperture z-scans to be performed without accurately knowing the characteristics of the beam.

$$(n_2)_s = \frac{E_r}{E_s} \frac{1 - R_r L_{\text{eff}}^r}{1 - R_s L_{\text{eff}}^s} \frac{\Delta T_{p-v}^s}{\Delta T_{p-v}^r} (n_2)_r \quad (4.1)$$

Here, the subscripts r and s denote parameters for the reference medium and sample medium, respectively. E is the optical energy used in the scan, R is the Fresnel reflectance, $(n_2)_s$ is the NLR coefficient of the sample under test, and $(n_2)_r$ is a trusted value for the NLR coefficient of the reference sample

Several glasses were used to test the reliability of the system for measuring n_2 , including Schott SF5, SF11, fused silica (FS), and SK11. These media were chosen because they do not exhibit significant NLA. Example data for SF5 are shown in Figure 4.1. Note that the data in red (T_{OA}) is from an open aperture z-scan and reveals a small but noticeable amount of NLA. This affects the closed aperture data by enhancing the valley and suppressing the peak. In calculating n_2 with ΔT_{p-v} , there would be no contributed error if the peak and valley offsets were equal, but this is not the case as is obvious in Figure 4.1.

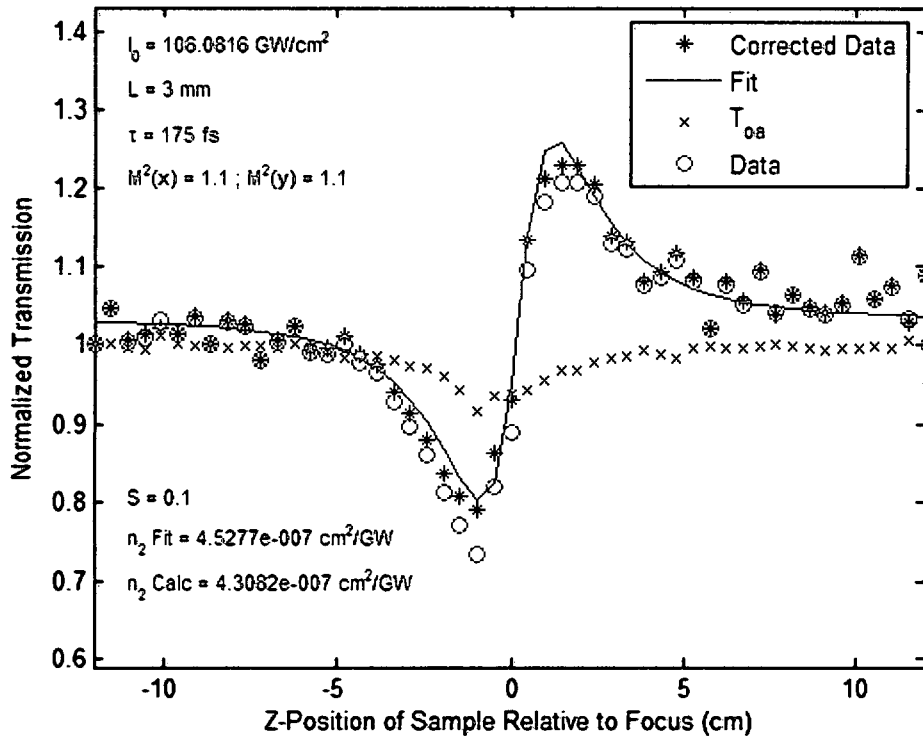


Figure 4.1 – Closed aperture z-scan data for SF11

The closed aperture data may be corrected as shown above using the open aperture data with Eq. (4.2), valid in the presence of “strong” NLA and provided both z-scans were performed at the same z-positions [16]:

$$T_{CA(\text{corrected})}(z) = T_{CA}(z) + [1 - T_{CA}(z)] \frac{1 - (1 - S)^{0.67}}{S} \quad (4.2)$$

Table 4.1 shows a comparison of measured and calculated values with predictions based on previous z-scan measurements performed under the same conditions. Calculations were executed using the measured ΔT_{p-v} value in Eq. (3.14). Since these values showed good agreement, closed aperture z-scans were trusted with confidence.

Table 4.1 – Comparison of data to previous results for n_2 reference media

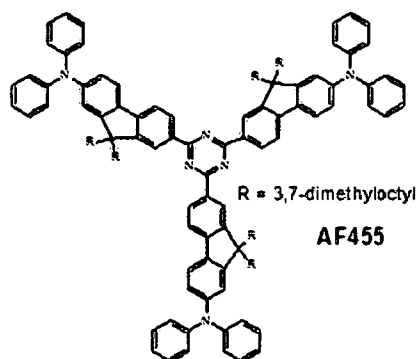
Medium	n_2 (cm ² /GW)		
	This Work		Previous Work [40]
	Fit	Calc	Calc
SF11	4.53E-7	4.31E-7	4.10E-7
SF5	2.76E-7	2.86E-7	2.60E-7
FS	5.97E-8	6.16E-8	6.0E-8
SK11	9.78E-8	1.07E-7	9.7E-8

4.2 Dyes & Solutions

The NLA properties of several liquid compounds were measured in this work, including AF455, Toluene, CS₂, RuPZn, RuPZnRu, NS-86-3, and NS-86-5. The NS-86 mixtures are two different solutions containing carbon nanotubes and their NLO properties are believed to be undocumented as well as the Ruthenium compounds. NLA properties were of primary concern for these media, and the concoction of these solutions was performed in an attempt to create strong nonlinearities.

4.2.1 AF455

The excited state absorption properties of AF455 were studied through several open aperture z-scans at different irradiances. The results are shown in Figures 4.2-4.5

**Figure 4.2** Molecular diagram of AF455 [44]

for the following beam parameters: $\lambda = 775$ nm, $M^2 = 1.1$; $w_0 = 73$ μm ; $\tau = 175$ fs; $L = 1$ mm. Figure 4.6 shows a summary of the β vs. irradiance as measured in Figures 4.3-4.5. These are presented to show the closeness of the fits between data and theory and are representative of data accuracy. Take note that the fits are extremely close for q_0 values well above unity.

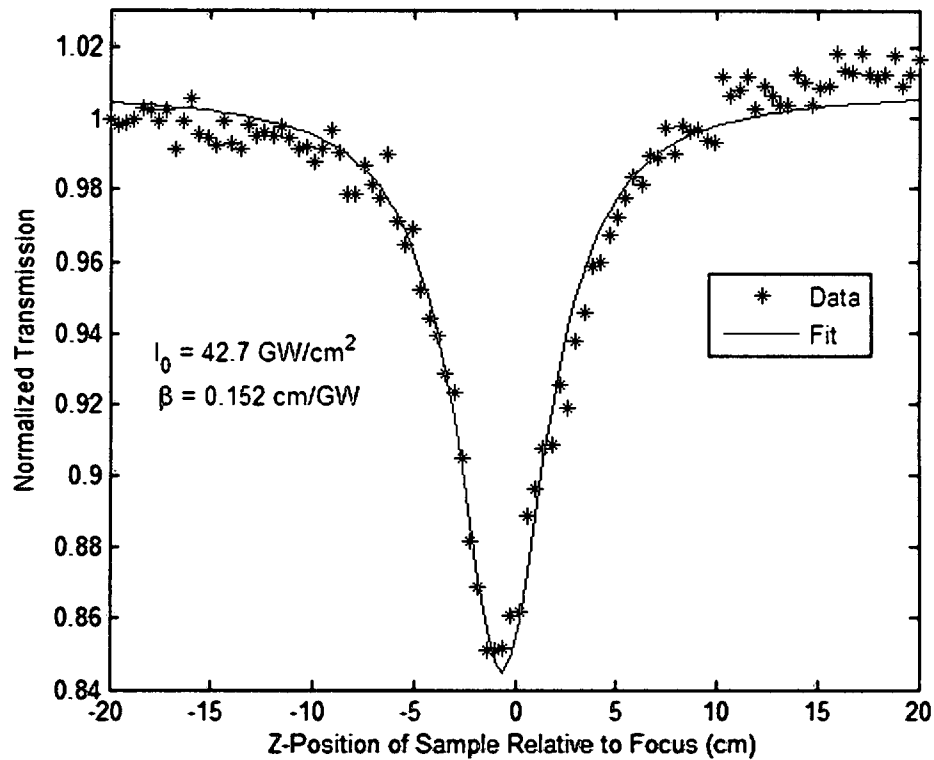


Figure 4.3 – Open aperture z-scan data for AF455 (1)

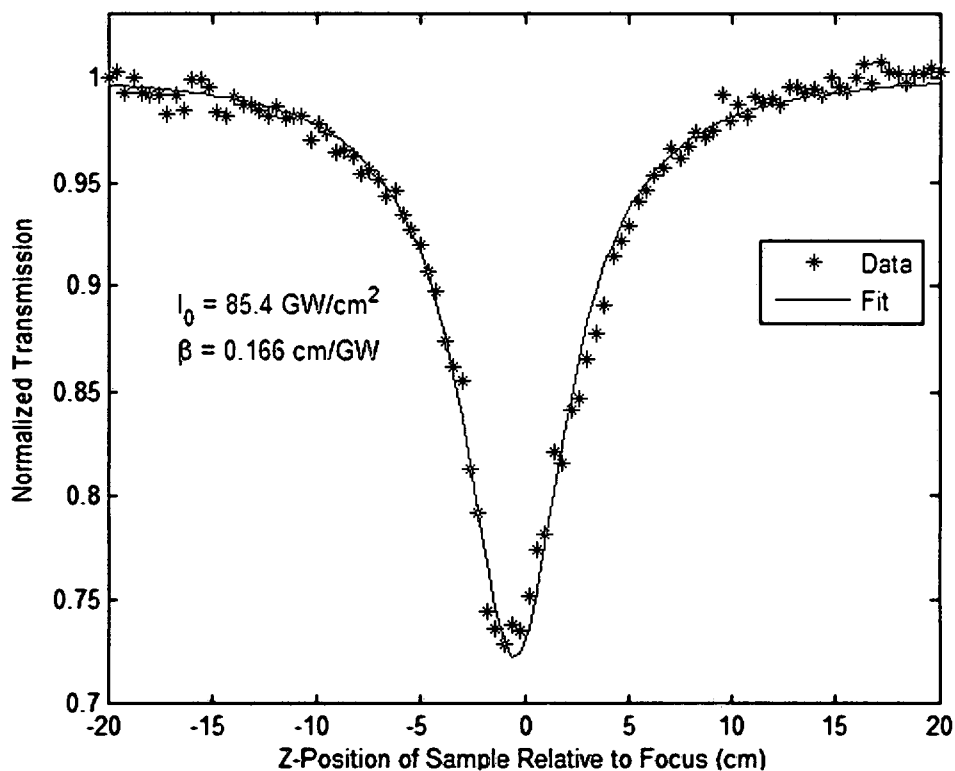


Figure 4.4 – Open aperture z-scan data for AF455 (2)

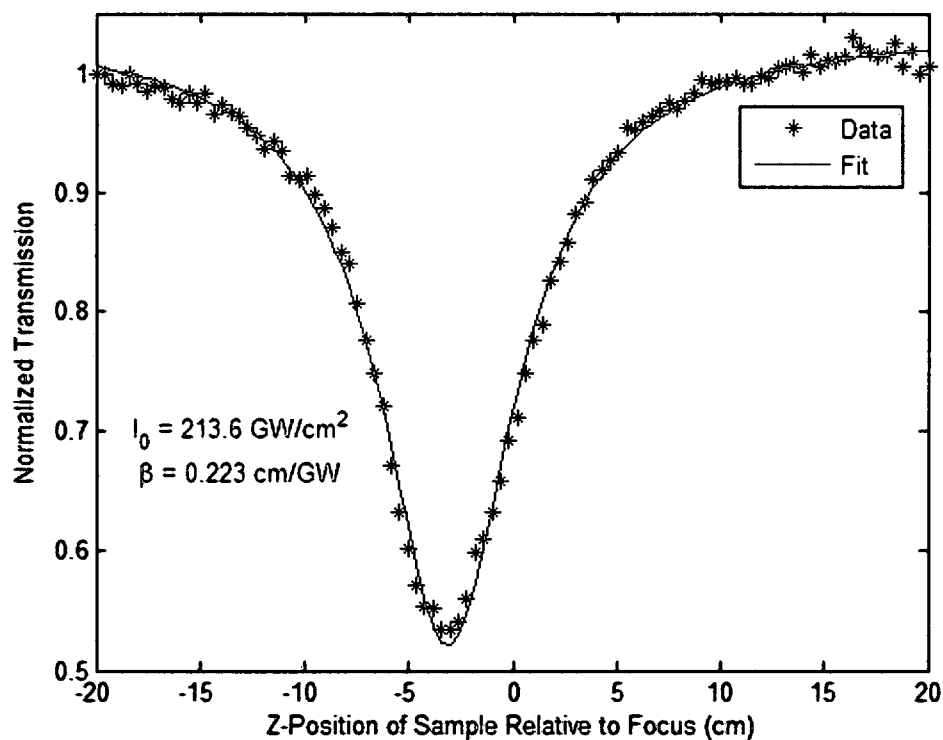


Figure 4.5 – Open aperture z-scan data for AF455 (3)

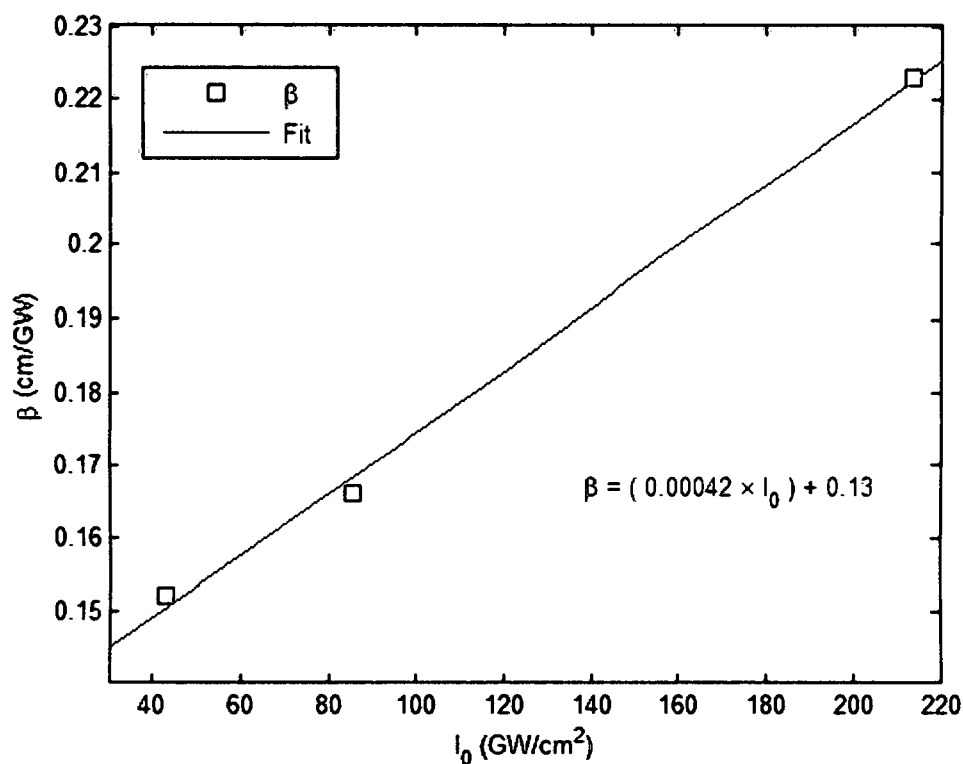


Figure 4.6 – ESA relationship with peak irradiance for AF455

4.2.2 Toluene

The NLA and NLR coefficients of Toluene were examined with this system under the following conditions: $\lambda = 775$ nm; $M^2 \cong 1$; $w_0 = 73$ μ m; $\tau = 175$ fs; $L = 1$ mm. This is a common solution used as a medium to support other materials and its molecular composition is shown in Figure 4.7. Its chemical formula is C_7H_8 .

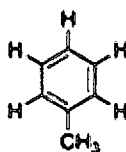


Figure 4.7 - Molecular diagram of Toluene [44]

Knowledge of the NLO properties of media such as this allows for the isolation of NLO contributions from other media that they may be mixed with. Results are shown in

Figure 4.8. Due to the magnitude of the irradiance used in these scans, the validity of the theoretical fits is stretched and therefore the error is as well. $\Delta\Phi_0$ is greater than π , forcing error beyond 5%. Although the absolute accuracy of the NLO coefficients is questionable, these data can be useful, nonetheless, as they show the reaction of the medium to an extreme irradiance.

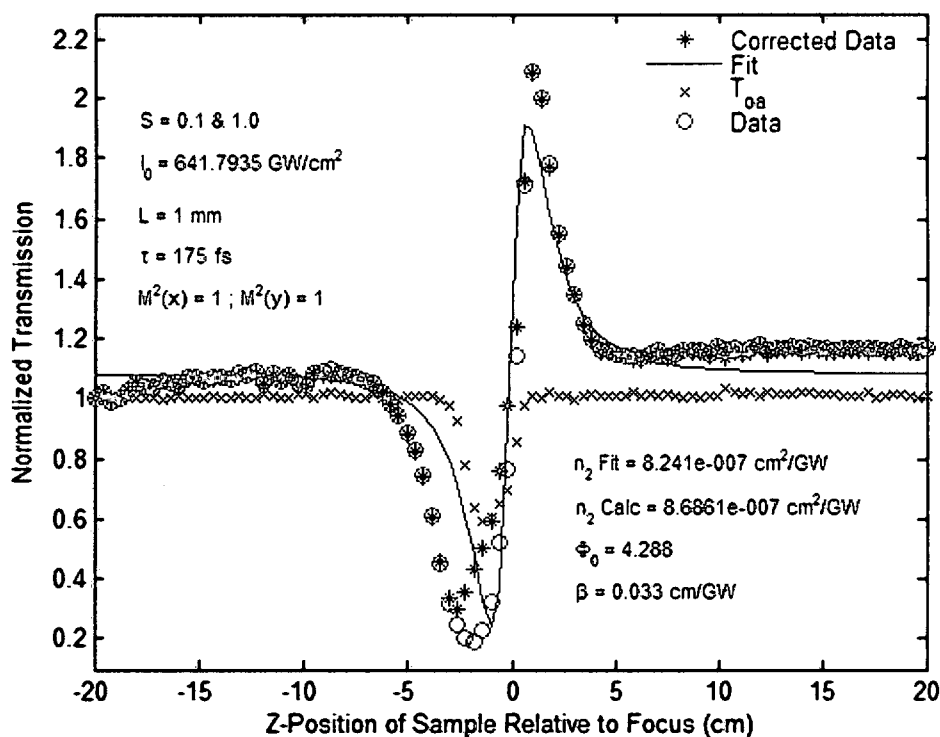


Figure 4.8 – Open & closed aperture z-scans of Toluene

4.2.3 Carbon Disulfide

CS₂ is by far the most common reference material used in NLO measurements; however it is argued that it is a poor choice for use with pulse widths below 200 femtoseconds due to high sensitivity of its NLO properties in this time scale [41].

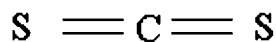


Figure 4.9 CS₂ molecular diagram

Open and closed aperture data are shown in Figures 4.10 and 4.11, respectively. The closed aperture z-scan data is uncharacteristic to theory and it is believed that thermal lensing or $\chi^{(>3)}$ effects are present. Thermal lensing can be ruled out if the repetition rate is significantly reduced and the closed aperture data doesn't change.

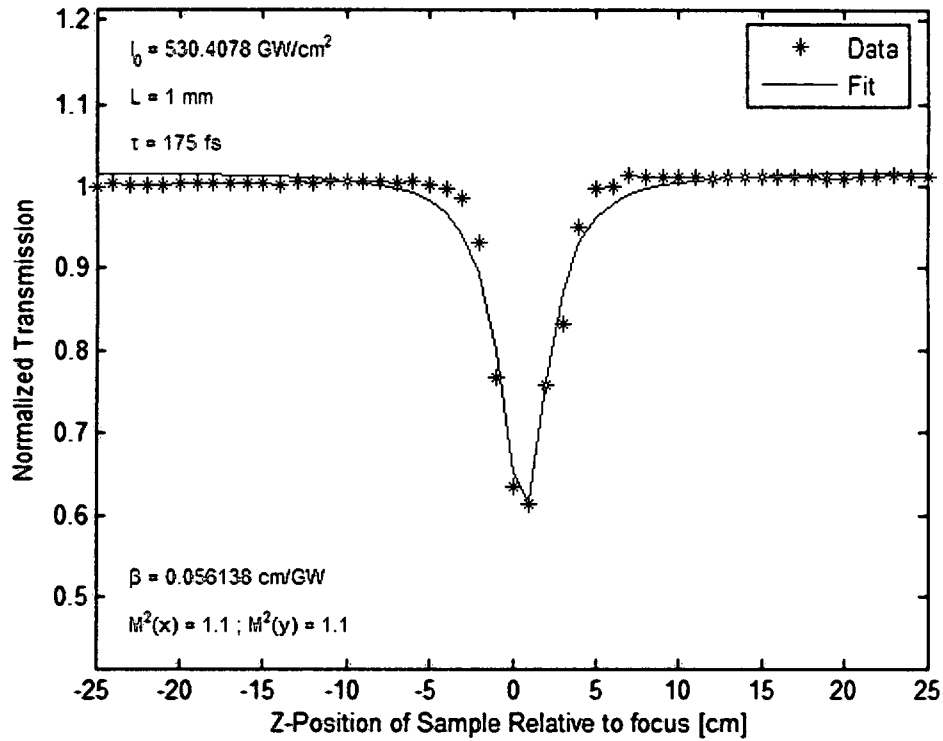


Figure 4.10 – Open aperture z-scan of CS₂

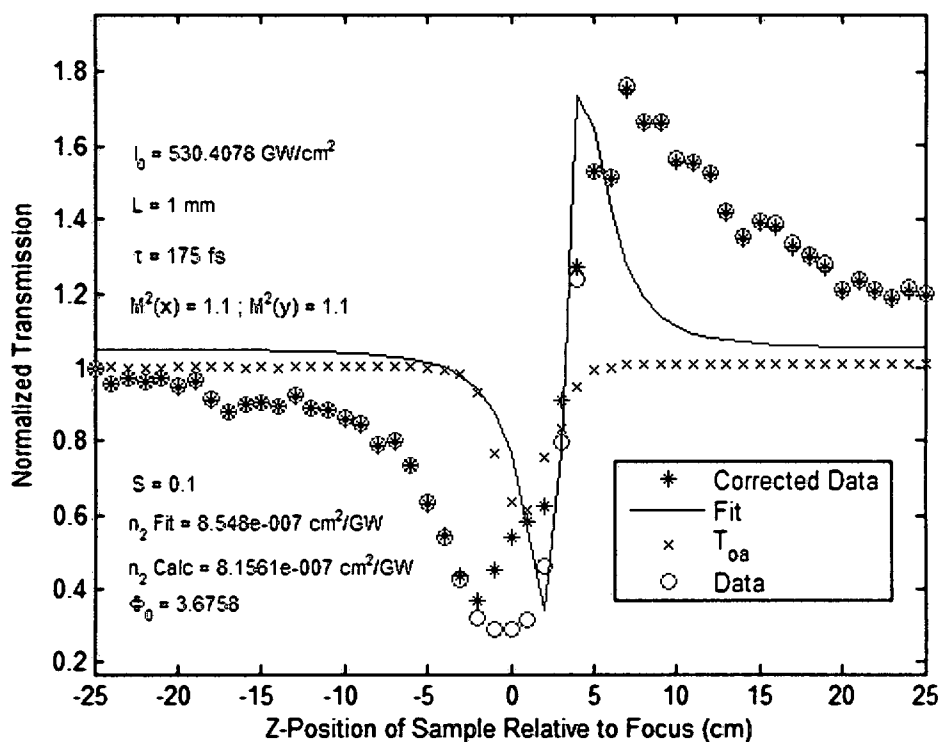


Figure 4.11 – Open & closed aperture z-scan of CS₂

4.2.4 RuPZn

NLR and NLA were measured for RuPZn as demonstrated in Figures 4.13-4.14 below. Excited state absorption was observed through several open aperture z-scans as well. A molecular depiction of this medium is shown in Figure 4.12.

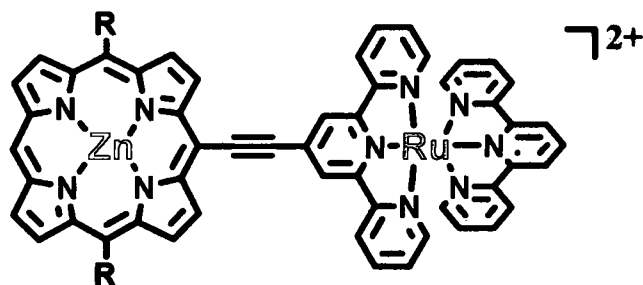


Figure 4.12 – Molecular diagram of RuPZn [44]

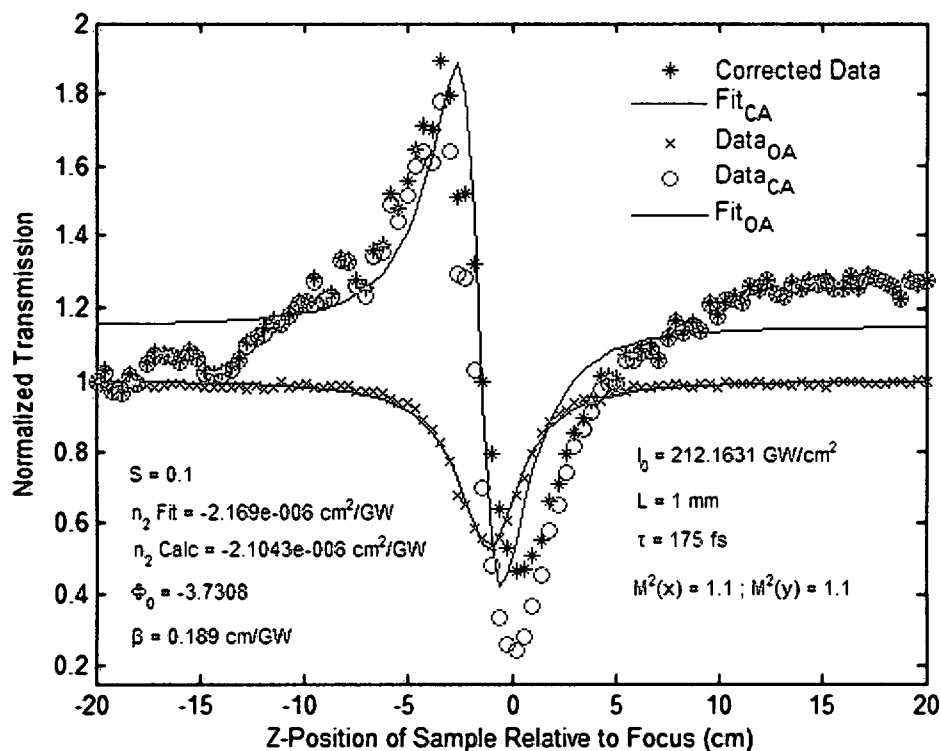


Figure 4.13 – Open & closed aperture z-scan of RuPZn

Here the peak precedes the valley (scanning from $-z$ to $+z$) in the closed aperture z-scan, revealing that RuPZn is a negative self focusing medium. Notice the shift in the baseline is nearly identical to that observed for CS₂ in Figure 4.8, although the two media have negative lensing effects. This is believed to be a thermal effect rather than beam walking from misalignment because these data were taken in short proximity to those taken of the glasses, in which the baselines were nearly ideal. A summary of the open aperture z-scans of RuPZn and the resulting ESA trend are shown below in Figures 4.14 and 4.15, respectively. Notice how the minimum transmission increases greatly with irradiance until it becomes very large ($> \sim 200 \frac{\text{GW}}{\text{cm}^2}$). It appears this medium reaches an absorption maximum of approximately 50%. This is believed to be the phenomenon of saturated absorption, described in Section 2.4, where the ground electronic state becomes depleted

of electrons and the medium is unable to absorb additional photons. It can be concluded from Figure 4.11 that ESA linearly contributes to the effective value of β for irradiances up to $\sim 200 \frac{\text{GW}}{\text{cm}^2}$, and thereafter other phenomena reduce β in an undetermined manner.

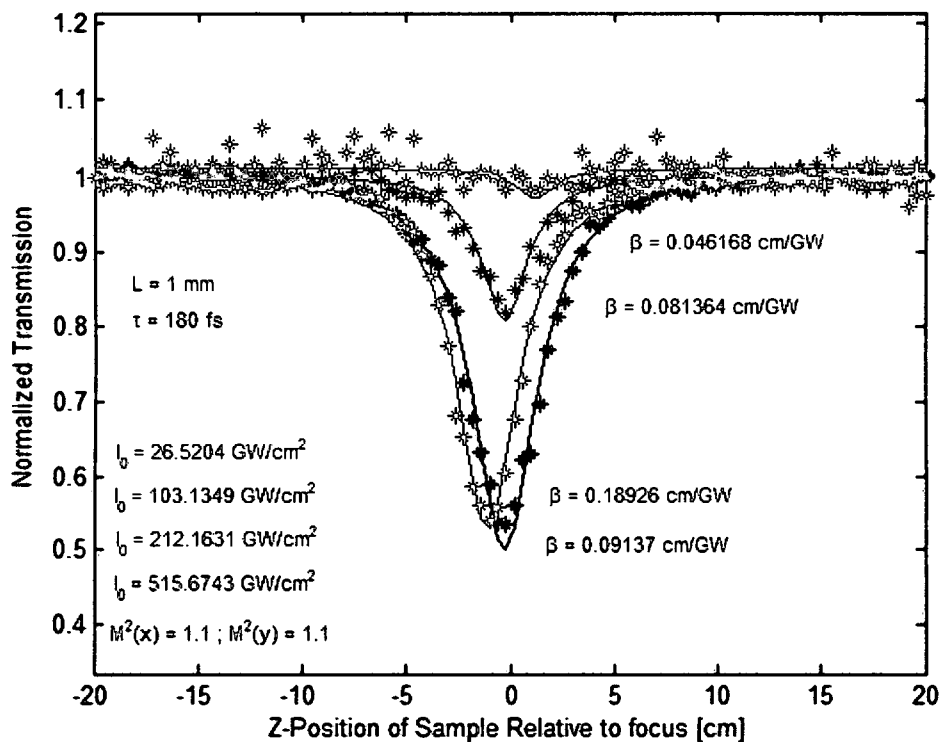


Figure 4.14 – Open aperture z-scans of RuPZn for various peak irradiances

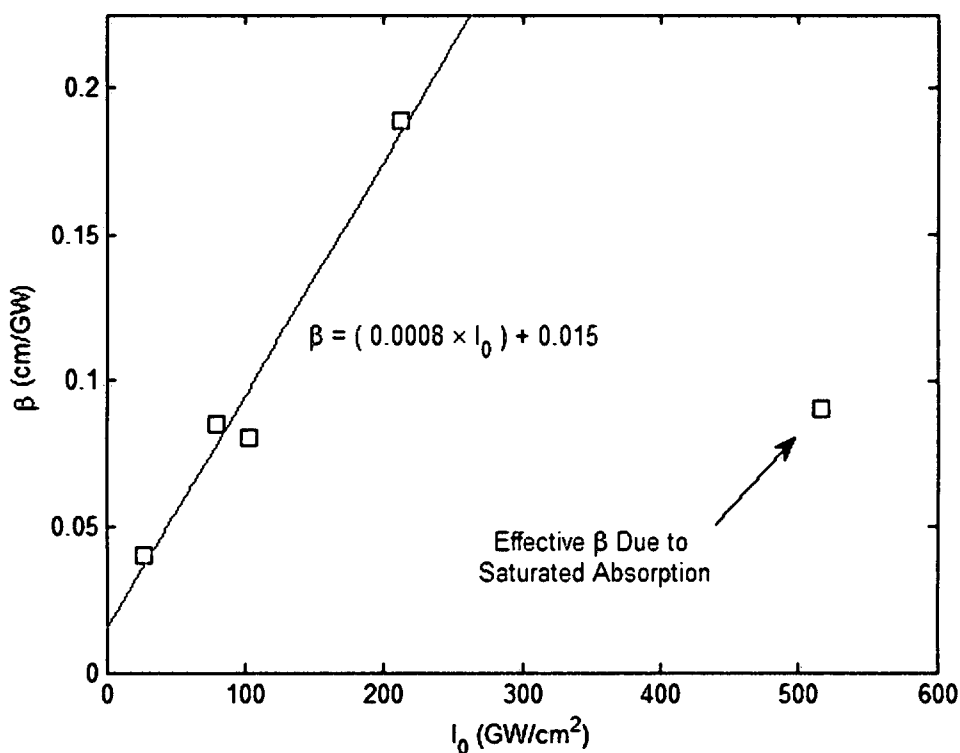


Figure 4.15 – ESA vs. peak irradiance for RuPZn

4.2.5 RuPZnRu

Another Ruthenium compound, RuPZnRu, was examined in the same manner. This showed to be roughly ten times more absorptive and also exhibited negative self-lensing. The results are shown in Figures 4.17 – 4.18, while the molecular diagram is shown in Figure 4.16.

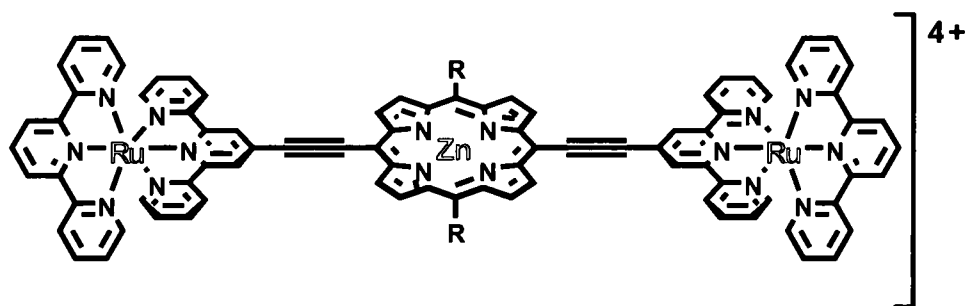


Figure 4.16 – Molecular diagram of RuPZnRu [44]

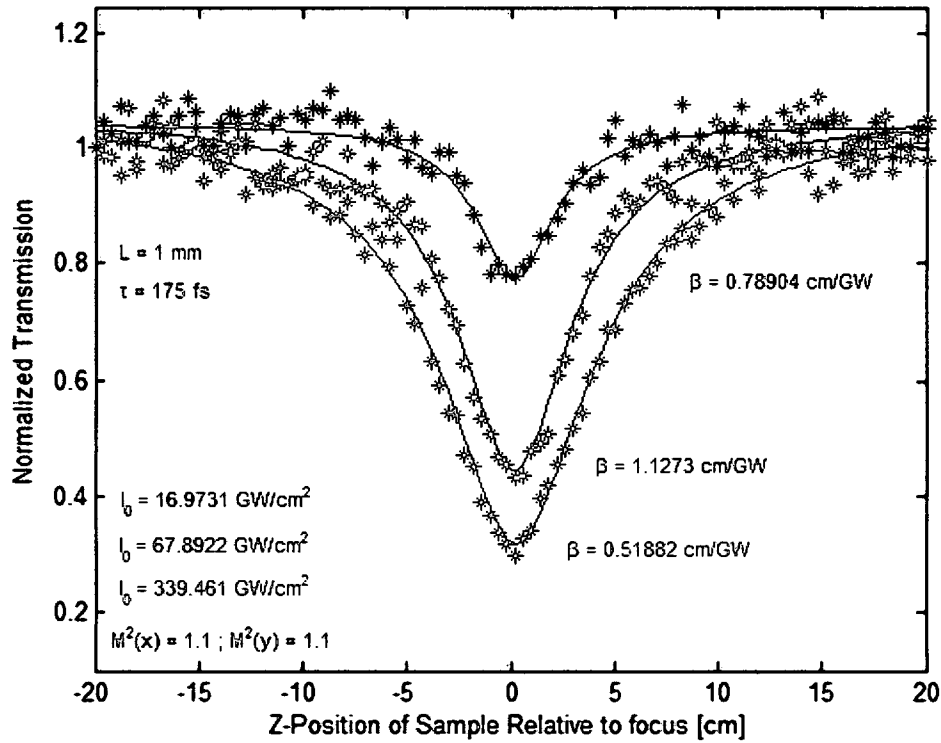


Figure 4.17 – Open aperture z-scans of RuPZnRu for various peak irradiances

Again, the theory was stretched for the closed aperture z-scan as shown in Figure 4.18. It may be of interest from a practical standpoint that the large combined contributions of NLR and NLA squelched the incident light almost entirely.

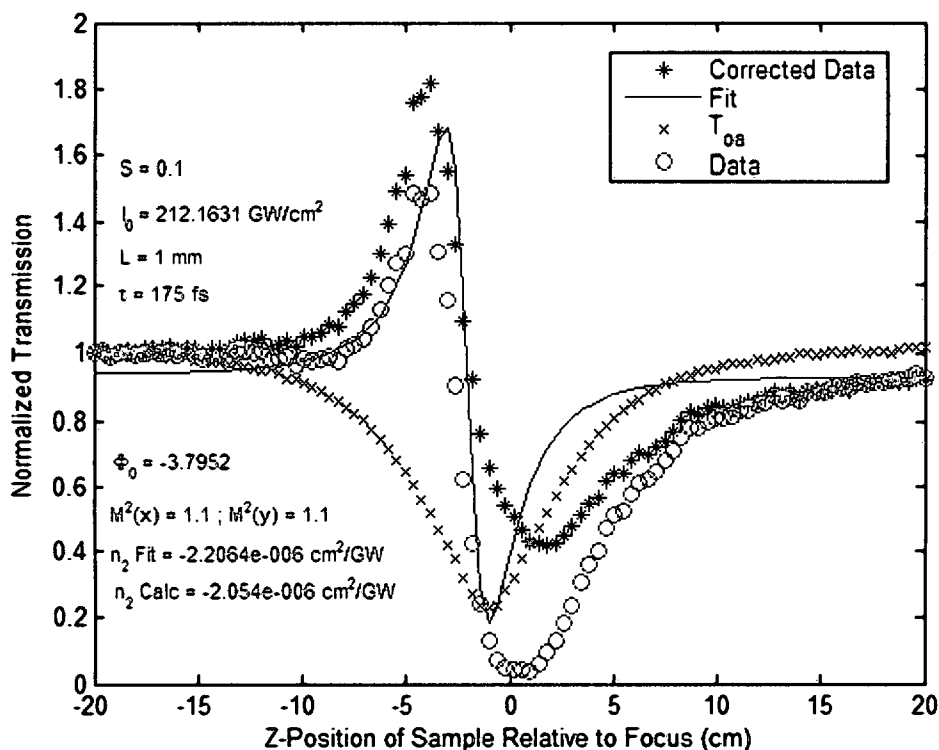


Figure 4.18 – Open & closed aperture z-scans of RuPZnRu

4.2.6 NS-86-3

This mixture of carbon nanotubes exhibited negative self-lensing as did the Ruthenium samples. The supporting solution was Toluene, which was characterized as shown in Section 4.2.2. The following data are results from the combined compound and the contribution from Toluene has not been isolated in determining the NLO coefficients. As can be seen in Figure 4.20, the β does not seem to follow an obvious trend with increased irradiance. This may be the result of combined error contributions from both high M^2 values and an insufficient number of data points. The theoretical curve uses exactly the same number of points as there are for data, and it is possible that the transmission minima went experimentally unobserved.

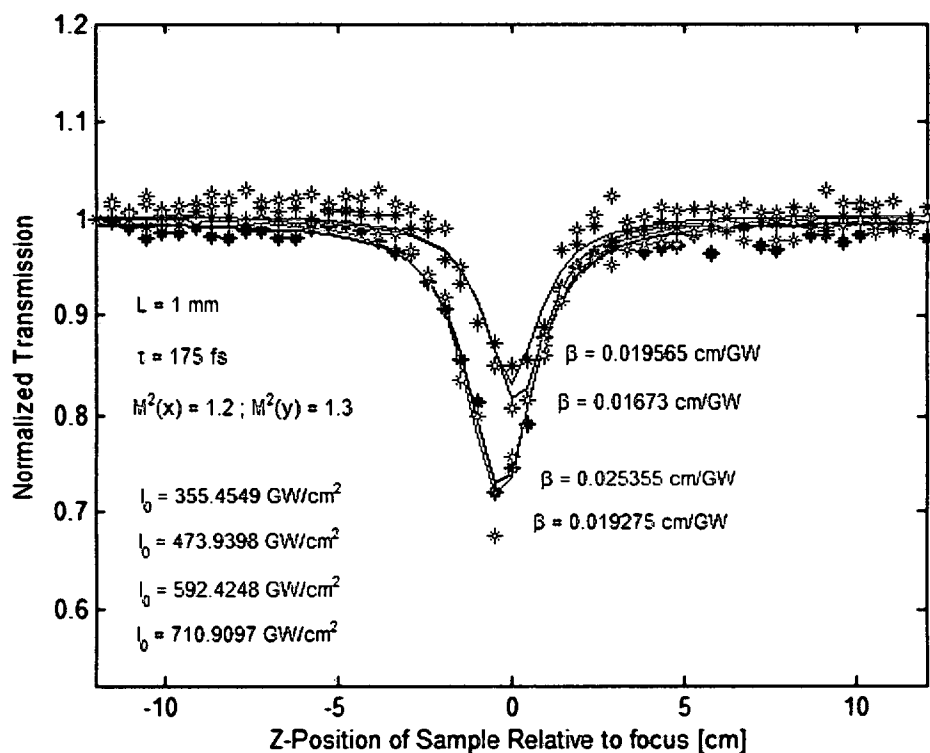


Figure 4.19 – Open aperture z-scans of NS-86-3

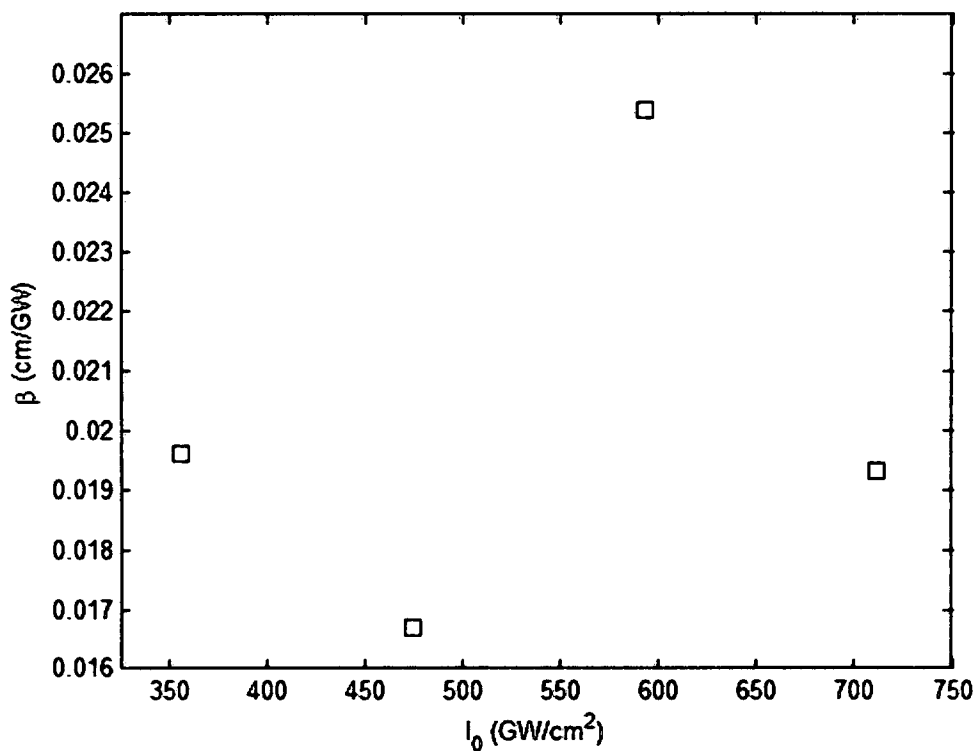


Figure 4.20 – Summary of NLA results for NS-86-3

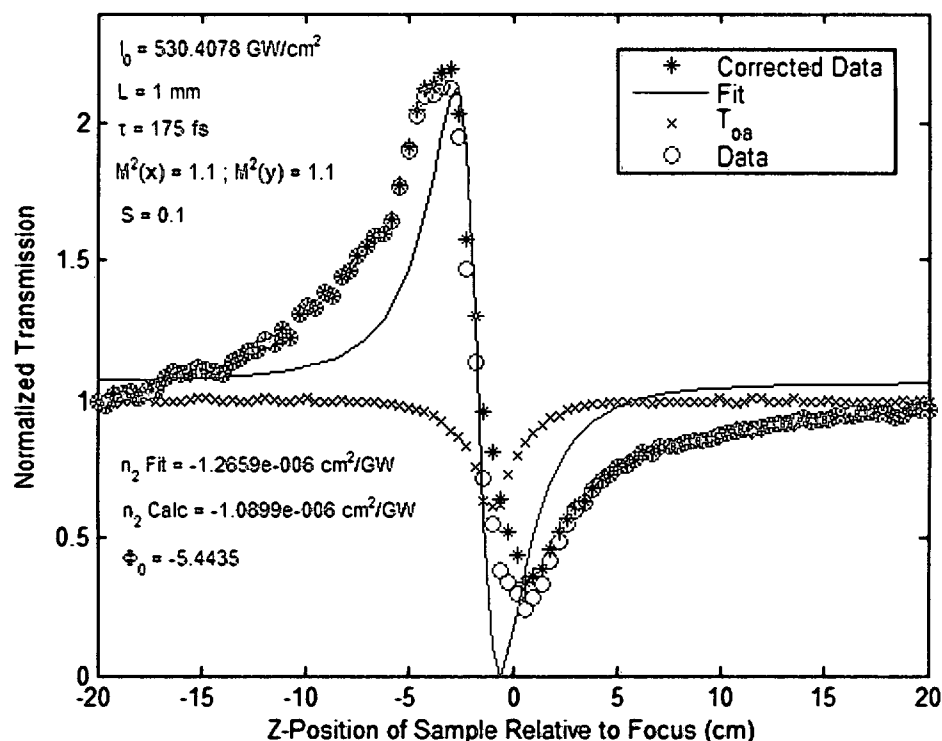


Figure 4.21 – Open & closed aperture data for NS-86-3

As seems to be the case for all liquid samples, the closed aperture trends yield inconclusive values for the NLR coefficient. The sign of n_2 is easily determined, however. Notice that the base solution, Toluene, is a positive self-lensing medium while the combination of Toluene and NS-86-3 is a strong negative self-lensing medium.

4.2.7 NS-86-5

This mixture of carbon nanotubes yielded similar NLA results to those of NS-86-3; however, they have opposite self-lensing effects. A summary of open aperture z-scans of NS-86-5 is provided in Figure 4.23. There appeared to be surface imperfections for this sample that affected both closed and open aperture data. This was remedied by performing z-scans at very low intensities (as to not trigger NLO mechanisms) and subtracting this data from high energy z-scans. This proved to be an effective method in normalizing out any deviations from the baseline not contributed by NLO activity.

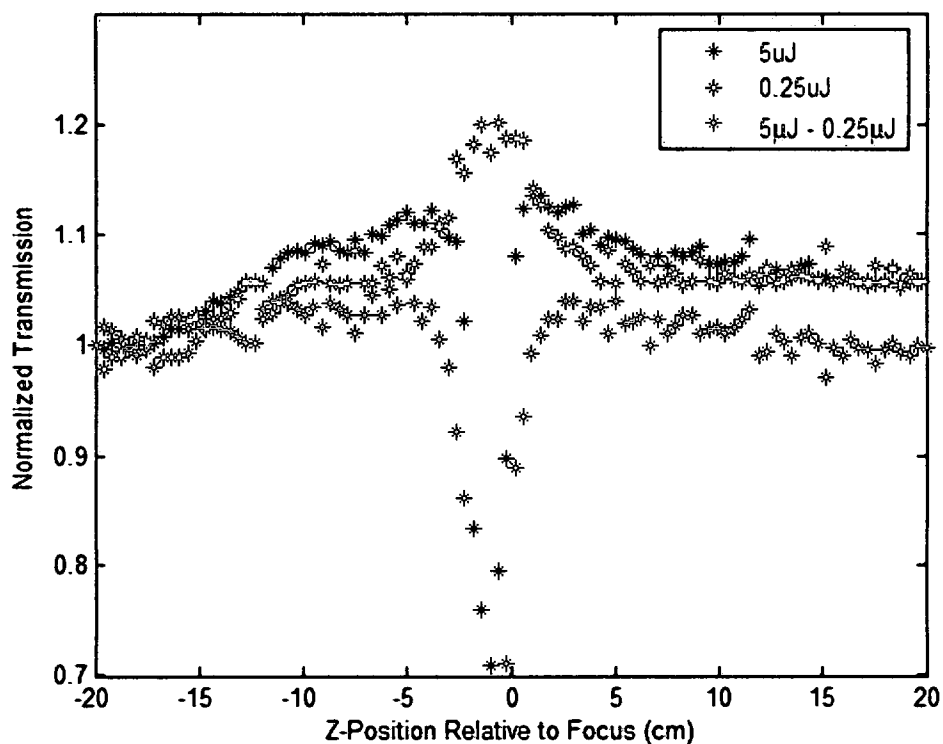


Figure 4.22 – The reduction of error due to sample imperfection

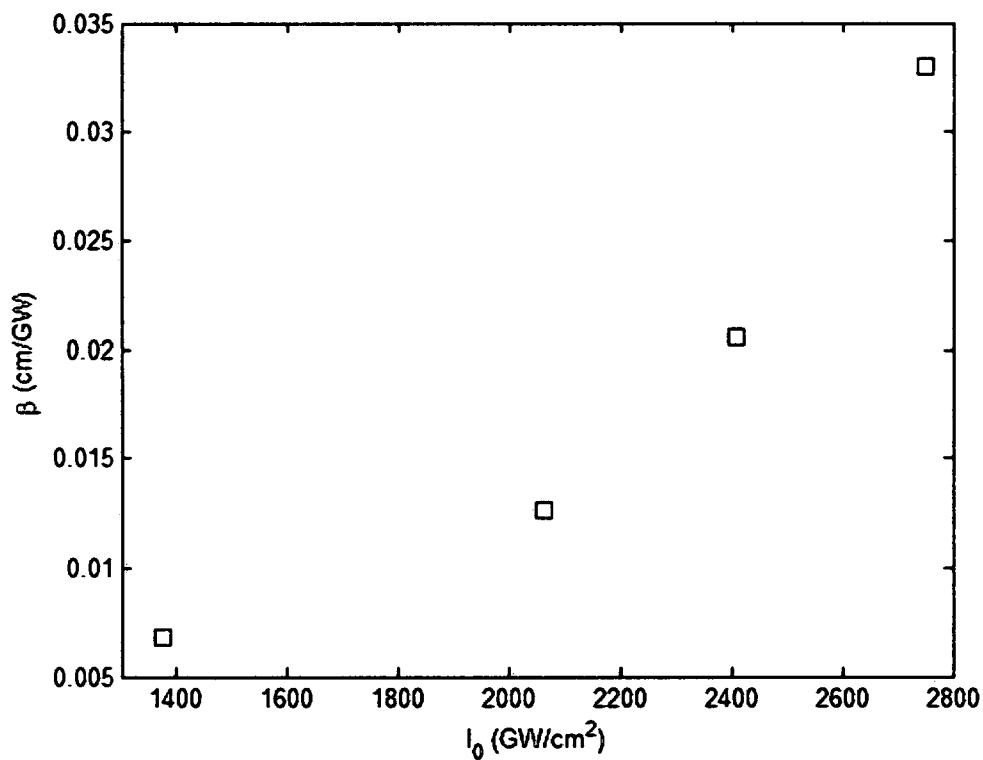


Figure 4.23 – Summary of NLA results for NS-86-5

The NLA coefficient in Figure 4.23 appears to be linear for higher irradiances, however the z-scan with the lowest irradiance resulted in a β that does not fit this trend. It is believed, but cannot be concluded with this work, that β is constant for $I_0 < 1400 \frac{\text{GW}}{\text{cm}^2}$ and that there is an ESA threshold in the proximity of $I_0 \cong 2000 \frac{\text{GW}}{\text{cm}^2}$.

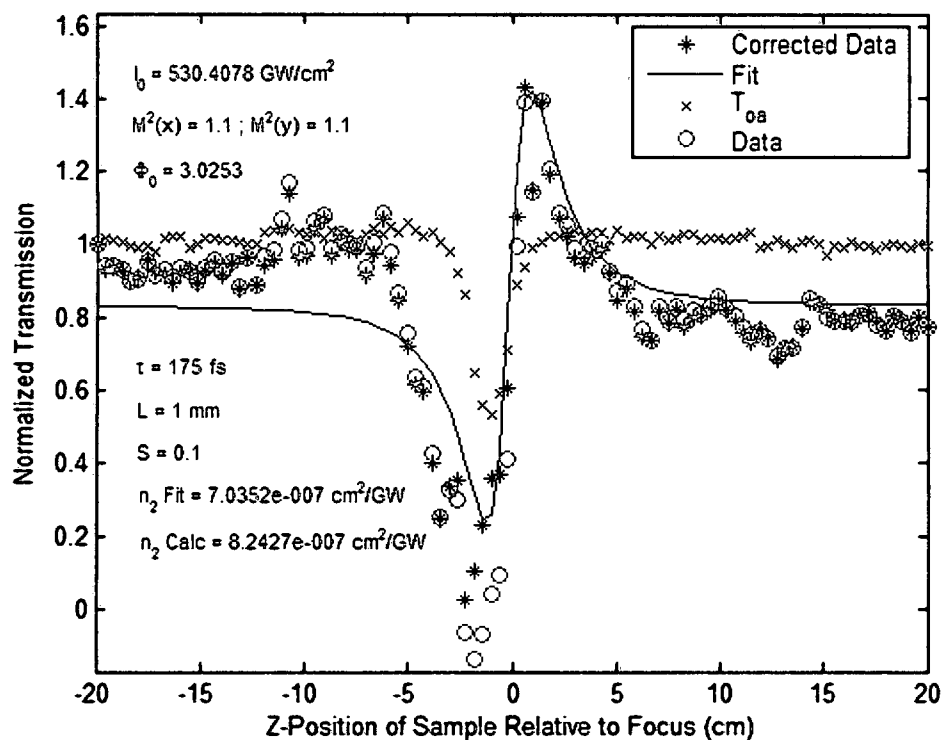


Figure 4.24 – Open & closed aperture data for NS-86-5

4.3 Thin Films

The thin films measured in this work include plasma enhanced chemical vapor deposited (PECVD) Benzene on BK7 substrates and PP-Benzonitrile (PP-BT) on B270 glass substrates. There were two PECVD-Benzene films; one high density (HD) and one low density (LD). The NLO properties of the substrates had to be measured so that their contributions could be eliminated from those of the films. It is unclear if NLO properties of these materials have been reported in this form.

4.3.1 PECVD Benzene

Benzene films roughly 1 μm thick were deposited onto 1 mm thick BK7 glass substrates. The molecular diagram for Benzene is shown in Figure 4.25.

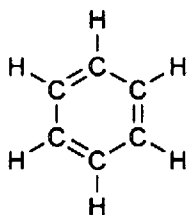


Figure 4.25 – Molecular diagram for Benzene [44]

Both the high and low density films exhibited no NLA in open aperture z-scans. Due to the very poor surface quality of these films, all data presented for these films were corrected by subtracting low energy z-scan data by high energy z-scan data as depicted below for closed aperture z-scans of the HD Benzene film. This is demonstrated in Figure 4.20. “Effective” measurements of the NLR coefficients are displayed in Table 4.2. These include the additive NLR contributions from the substrates and films. The value obtained for BK7 agrees excellently with commonly reported values in the range of $3 \times 10^{-7} \frac{\text{GW}}{\text{cm}^2}$ to $3.4 \times 10^{-7} \frac{\text{GW}}{\text{cm}^2}$.

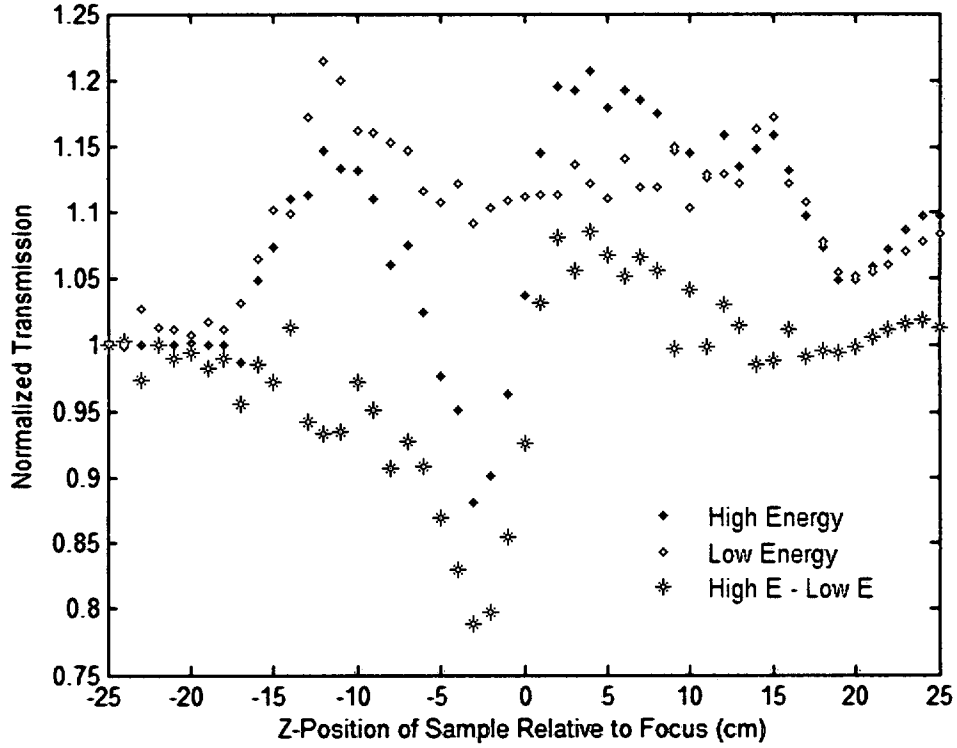


Figure 4.26 – Reducing error from surface imperfections in a closed aperture z-scan

Table 4.2 – Effective n_2 values from closed aperture z-scans

Medium	BK7 (3 mm)	HD (1 μm) +BK7 (1 mm)	LD (1 μm) +BK7 (1 mm)
n_2 (cm^2/GW)	3.201E-7	2.323E-7	2.798E-7

By rearranging Eq. 3.14 and fixing n_2 to that measured for BK7, it can be shown that the sample thickness is directly proportional to ΔT_{p-v} , and therefore n_2 :

$$\Delta T_{p-v} \cong n_2 0.406(1 - S)^{0.25} k I_0(t) L_{\text{eff}} \quad (4.3)$$

$$\Delta T_{p-v} \cong (\text{const}) \times L_{\text{eff}} \quad (4.4)$$

With this the NLR coefficient for a 1 mm thick sample of BK7 can be deduced from that measured for the 3 mm thick sample through a simple division:

$$n_2(\text{BK7: 1 mm}) = \frac{n_2(\text{BK7: 3 mm})}{3} \quad (4.5)$$

This results in an NLR coefficient of $1.067\text{E-}7 \text{ cm}^2/\text{GW}$. Subtracting this from the effective values for the film-substrate combinations above, the NLR contributions of the films are isolated from the substrate. These values are presented in Table 4.3.

Table 4.3 – Isolated n_2 values from closed aperture z-scans

Medium	BK7 (1 mm)	HD (1 μm)	LD (1 μm)
$n_2 \text{ (cm}^2/\text{GW)}$	1.067E-7	1.256E-7	1.731E-7

4.3.2 Polyphenylene-Benzonitrile (PP-BT)

Six variations of this film were examined for NLA and NLR properties. The substrates were 2 mm thick disks of B270 glass and the film thicknesses were roughly 1 μm . Shown in Figure 4.27 are open aperture data superimposed for all six films. The NLA is insignificant for all films. The NLR coefficient was extracted from a closed aperture analysis on a film-free sample of B270 as shown in Figure 4.28.

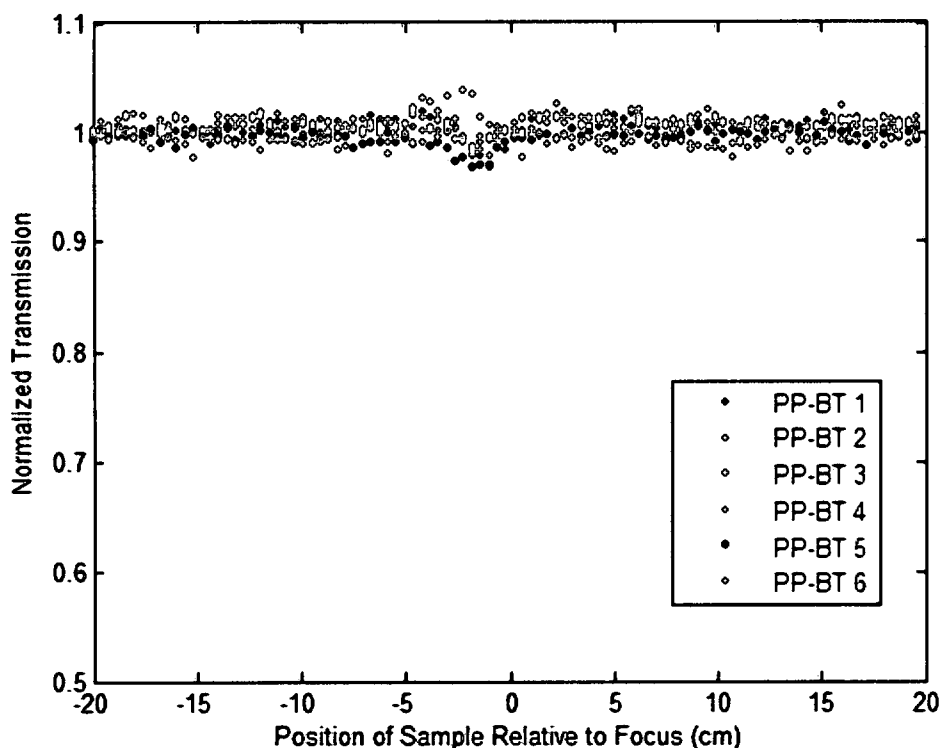


Figure 4.27 – Open aperture z-scans of all PP-BT films

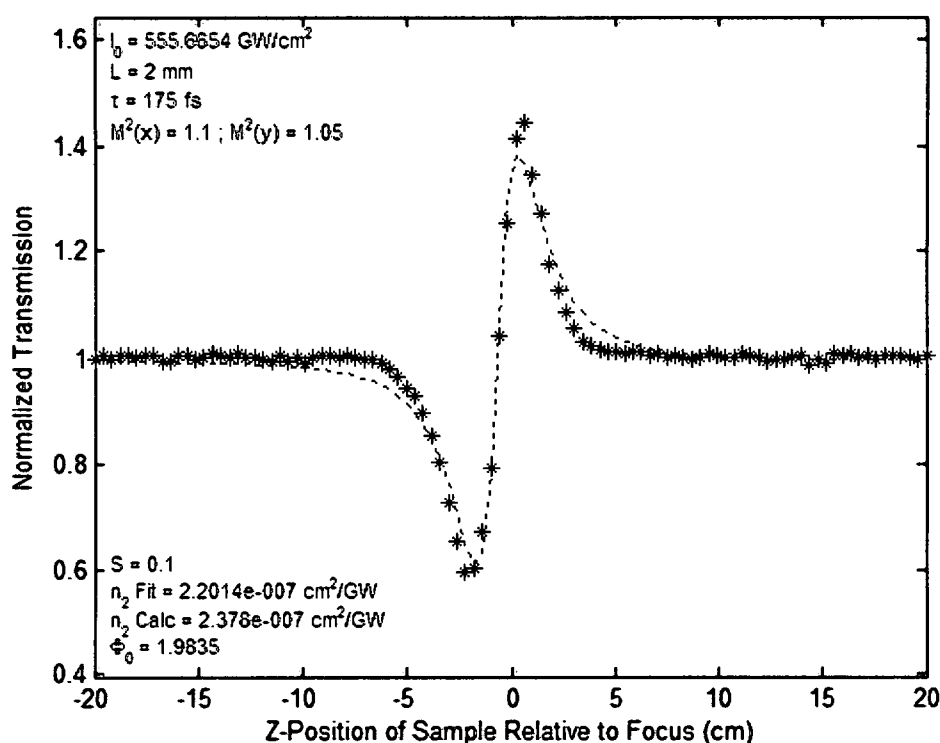


Figure 4.28 – Closed aperture z-scan of the substrate, B270

Closed aperture z-scans were performed on all the films as well; however there was no hint of NLR properties from any of the films. Point to point, the data from every closed aperture z-scan followed the trend of Figure 4.28 above almost exactly when superimposed. The presence of NLR in the films would not have followed the data from that of the substrate so closely. Example data are shown below in Figure 4.29.

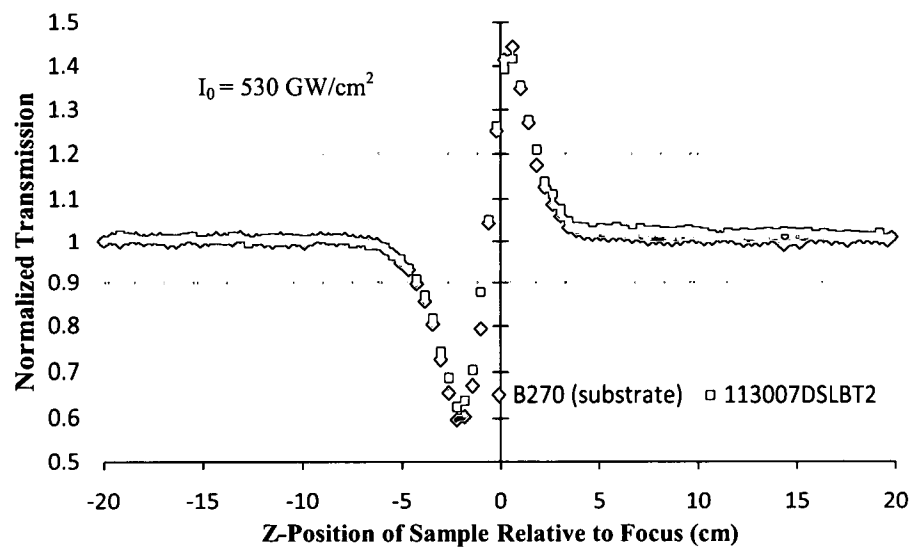


Figure 4.29 – Example of negligible NLR effect of PP-BT films

4.4 Data Summary

Tabulated below is a summary of NLA and NLR coefficients obtained from the z-scan NLO measurement system and post-scan analyses. All values reported here were taken with $\lambda = 775$ nm, $\tau = 175 \pm 10$ fs, and a repetition rate of 500 Hz. Reference values have similar experimental parameters.

Table 4.4 – Summary of NLO data for various optical media

Medium	β (cm/GW) Measured	β (cm/GW) Ref	n_2 (cm ² /GW) Measured	n_2 (cm ² /G W) Ref
AF455	0.152-0.223		-	-
B270	~0	-	2.16E-07	-
BK7	~0	-	3.2E-07	3-3.4E-7
C-P5972	0.88	-	-	-
CS ₂	0.06	-	3.07E-06	30E-6
Fused Silica	-	0.042	5.54E-08	6E-8
KCl	0.0021		-	1.7E-7
NS-86-3	0.023	-	Negative	-
NS-86-5	0.0068	-	Positive	-
PECVD-Benzene HD	~0	-	2.323E-7	-
PECVD-Benzene LD	~0	-	1.731E-7	-
PP-Benzonitrile	~0	-	~0	-
RuPZn	0.084	-	Negative	-
RuPZnRu	0.79	-	Negative	-
SF11	0.0092	-	4.42-4.62E-7	2.18E-7
SF5	-	-	2.62E-07	2.26E-7
SK11	~0	-	9.22-9.67E-8	-
Soda Lime Glass	~0	-	2.25E-07	-
Toluene	0.0081	-	1.00E-06	9.8E-7
ZnSe	8.67	5.8	-	1E-5

CHAPTER 5

Conclusions

In this work, a NLO materials characterization system was built based on that introduced by Sheik Bahae *et al.* The optics and other experiment parameters were chosen based on designs accommodating theoretical limitations and realistic assumptions of samples to be characterized. Measurements were taken to reduce the error of the system through beam filtering, averaging, and normalizing out power fluctuations. A master control program was written to automate measurement processes and data acquisition. Programs were also written to automate energy and detector calibration routines, which fed results to the master program. In addition, automated curve fitting analyses were generated, allowing large flexibility of experimental conditions and data correction. The use of these analyses is not limited to this system and may be easily used with data from any z-scan test bed.

Once proven to generate reliable results, this system was used to test a variety of optical media. These included thin films, liquids, and solids, several of which currently not having documented NLO properties. Excited state absorption was observed in some media as well as saturated absorption. It is possible to extract ESA cross sections from z-scan measurements; however, this was out of the scope of this work. The interest here was not to measure the absolute NLO contributions from various mechanisms, but rather

the general, or effective, radiation-matter effects as would be of interest from an applications standpoint.

It was noticed that the liquid samples yielded poor NLR data. The sign of the n_2 was easily determined, but the closed aperture z-scan data were commonly erratic relative to theory. This is believed to be due to cumulative thermal effects, a function of the repetition rate of the laser. A simple remedy might be the addition of a delay between data acquisitions. Other solutions include reducing the pulse repetition rate by adding optical chopper wheels.

This system proved to be an accurate as well as rapid NLO measurement tool. The time between data acquisitions at different z-positions was approximately 2.5 seconds. A typical z-scan consisted of 50-100 points, taking ~2-4 minutes from start to finish. The addition of a third detector would make it possible to simultaneously perform open and closed aperture z-scans by placing a beam splitter between the signal detector and sample. The curve fitting algorithms had computation times of < 30 seconds for both open and closed aperture analyses. A complete characterization of the effective NLR and NLA coefficients of a medium can be performed in less than 10 minutes with this system, making it useful for quickly screening new materials. Another benefit of the speed of this system is the practicality of performing experiments where n_2 or β need to be known for many values of some experimental parameter, such as wavelength. This was the motivation for using photodetectors instead of a CCD camera. Data acquisition with the photodetector-oscilloscope combination is many times quicker than it would be with a CCD camera due to integration time and averaging. The accuracy and sensitivity of the system could be improved by using a CCD camera for several reasons. Pointing stability

would not be an issue because software could synthetically aperture the beam while adjusting for a moving centroid. Spatial distortions of the beam would be noticed real-time, and other variations of the z-scan method may be implemented, such as the EZ-scan [28]. This would also allow the simultaneous acquisition of open and closed aperture z-scan data.

In future experiments, an optical parametric amplifier (Light Conversion Ltd. TOPAS-C) will be used as laser source for this system, continuously tunable from approximately 532 nm to 12 μm . This will undoubtedly pose problems for closed aperture z-scans if the system is left as is. The silver mirrors are highly reflective in this wavelength range, but the refractive optics (BK7) are dispersive and their effective focal lengths change as a function of wavelength as is demonstrated in Figure 5.1. This may lead to an unacceptable loss of light through the spatial filter.

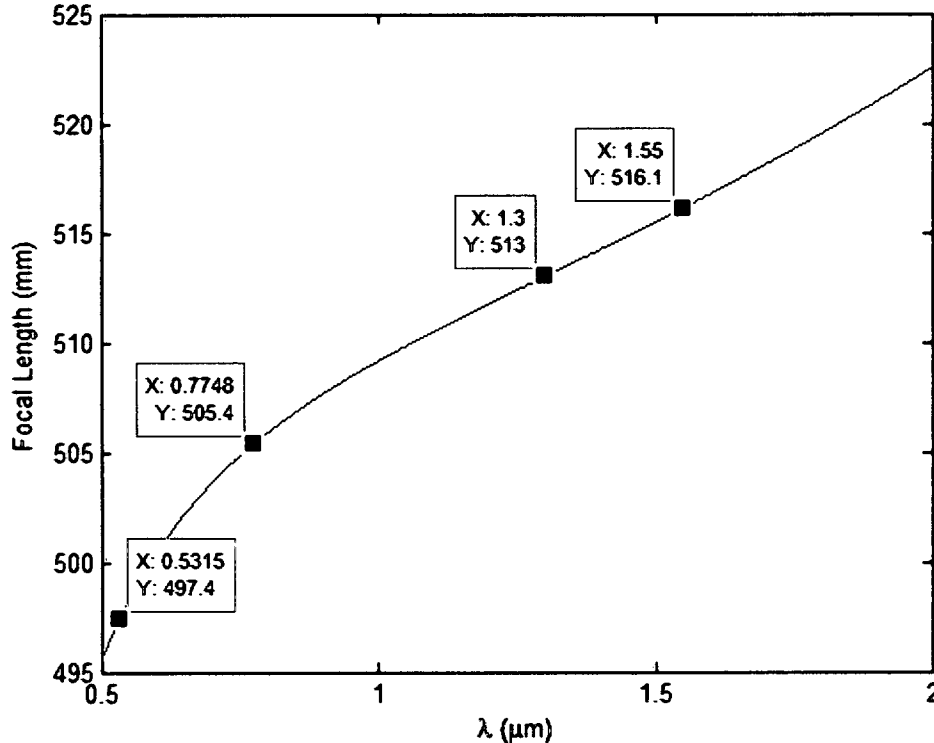


Figure 5.1 – Focal length of L_3 vs. wavelength

Replacing the refractive optics with reflective optics would keep the focal lengths in place, the only change being the spot sizes at foci. The TOPAS should be first characterized at many wavelengths, for a spatial filter may not be necessary after all.

The optics composing the attenuator will need to be replaced with those capable of attenuating a broader range of wavelengths and auto-correlator measurements should be taken in the sample path to account for pulse spreading from optics between the sample and laser. This is more apparent in shorter pulses, and the TOPAS can output pulses enduring half as long as the input pulses.

A program was written to control the wavelength of the TOPAS and can be incorporated into the master z-scan program. This would allow a user to perform automated nonlinear spectroscopy on materials as a function of both wavelength and irradiance. Another step that would be beneficial would be real-time data analysis. It may not always be obvious that data is erroneous until well after an experiment is changed.

APPENDIX A

Matlab Curve Fitting Algorithms

```
%%%%%%%%%%%%%%%%%%%%%%%%%%%%%%%%%%%%%%%%%%%%%%%%%%%%%%%%%%%%%%%%%%%%%%%%
% Geoffrey D. Jenkins - University of Dayton - WPAFB, OH - April 2008 %
%
% File name: oafita.m
%
% This is the first of 2 m-files needed for performing automated
% curve fits to open aperture z-scan data. This is the only file that
% needs to be run. It operates on the 2nd m-file, oafitb.m, which
% needs to be in the same directory as this file.
%%%%%%%%%%%%%%%%%%%%%%%%%%%%%%%%%%%%%%%%%%%%%%%%%%%%%%%%%%%%%%%%%%%%%%%%

% Clears Matlab variables and closes all open figures
clear all
close all
% These are the initial guesses for beta, y-offset, and x-offset,
% respectively
guess = [0.1*1e-2/1e9, 0, 0];
% Data file is loaded, Matlab searches for the data file in the same
% directory as the m-files. MS Excel format assumed.
datafile = xlsread('Data File Name');
% Sets column 5 of the data file to the variable 'data'. Column 5 is
% the current location of the Normalized Transmission data as formatted
% in LabVIEW
data = datafile(:,5)';
% Loads beam parameters from column 6 of the datafile. This is the
% current location as formatted by the LabVIEW z-scan program
global params;
params = datafile(:,6);
% Assigns all experimental parameters to appropriate Matlab variables
S = params(6); % Linear transmission of aperture
L = params(2)*1e-3; % Sample thickness
E = params(11)*1e-6; % Beam energy
lambda = params(3)*1e-9; % Wavelength
k = 2*pi/lambda; % Wavenumber
f = params(1)*1e-3; % Focal length
M2x = params(9); % Divergence imperfection factor, x-dimension
M2y = params(10); % Divergence imperfection factor, y-dimension
Dx = params(4)*1e-3; % Diameter of the beam at focusing lens, x-
% dimension
Dy = params(5)*1e-3; % Diameter of the beam at focusing lens, y-
% dimension
wox = (2.*lambda.*f.*M2x)./(pi.*Dx); % Beam waist @ focus, x-dimension
woy = (2.*lambda.*f.*M2y)./(pi.*Dy); % Beam waist @ focus, y-dimension
```

```

zox = params(7)*1e-3; % Location of wox rel. to focal plane
zoy = params(8)*1e-3; % Location of woy rel. to focal plane
zo = (pi*((wox+woy)/2)^2)/lambda; % Approximate Rayleigh range
zrx = (pi.*wox.^2)/(lambda.*M2x); % Rayleigh range, x-dimension
zry = (pi.*woy.^2)/(lambda.*M2y); % Rayleigh range, y-dimension
tau = params(12)*1e-15; % Pulse width
Io = (0.56*E)/(wox*woy*tau); % Peak irradiance
start = params(15)*1e-2; % Start position of sample rel. to focus
finish = params(16)*1e-2; % Ending position of sample rel. to focus
pts = params(17); % # data points
% Unconstrained Nonlinear Optimization function that loads 2nd m-file
[beta,fval,eflag] =
fminsearch(@(beta)oafitb(beta,data),guess,optimset('MaxFunEvals',50000,
'MaxIter',50000))
% Takes variables from fit and loads them into theoretical equation
for n = 1:pts
    z = start + (n-1)*(finish-start)/pts;
    sol(n) = beta(2)+((pi.*wox.*sqrt(1+((z+beta(3)-
zox).^2)./zrx.^2)).*woy.*sqrt(1+((z+beta(3)-
zoy).^2)./zry.^2)).*tau)/(2.*beta(1).*L.*(2.*log(1+sqrt(2)))).*E)).*quad
(@(x)log(1+(beta(1).*L.^2.*log(1+sqrt(2)).*E.*(sech(x)).^2)/(pi.*wox.*
sqrt(1+((z+beta(3)-zox).^2)./zrx.^2)).*woy.*sqrt(1+((z+beta(3)-
zoy).^2)./zry.^2)).*tau)),-10,10);
end

global beta;
beta = beta(1)/(1e-2/1e9);
global qo;
qo = Io/1e13*L/1e2*beta;
% Plots theoretical curve using variables extracted from fit
z = linspace(start,finish,pts);
plot(z*100,data,'*',z*100,sol)
set(gcf,'DefaulttextFontSize',8)
legend('Data','Fit')
xlabel('Z-Position of Sample Relative to focus [cm]')
ylabel('Normalized Transmission')
text(z(3)*100,(max(data)+0.15),['I_0 = ' num2str(Io/1e13) ' GW/cm^2'])
text(z(3)*100,(max(data)+0.15)-0.055,['L = ' num2str(L*1000) ' mm'])
text(z(3)*100,(max(data)+0.15)-0.11,['\tau = ' num2str(tau*1e15) ' fs
'])
text(z(3)*100,(min(data)-0.2)+0.165,['q_0 = ' num2str(qo)])
text(z(3)*100,(min(data)-0.2)+0.11,['\beta = ' num2str(beta(1)) '
cm/GW'])
text(z(3)*100,(min(data)-0.2)+0.055,['M^2(x) = ' num2str(M2x) ' ;
M^2(y) = ' num2str(M2y)])
axis([start*100 finish*100 (min(data)-0.2) (max(data)+0.2)])

```



```

%%%%%%%%%%%%%%%%%%%%%%%%%%%%%%%%%%%%%%%%%%%%%%%%%%%%%%%%%%%%%%%%%%%%%%%%
% Geoffrey D. Jenkins - University of Dayton - WPAFB, OH - April 2008 %
%
% File name: oafitb.m
%
% This is the 2nd of 2 m-files needed for performing automated
% curve fits to open aperture z-scan data. This m-file is a function
% called by oafita.m
%%%%%%%%%%%%%%%%%%%%%%%%%%%%%%%%%%%%%%%%%%%%%%%%%%%%%%%%%%%%%%%%%%%%%%%%

```

```
function f = oafitb(beta,data)
```

```
global params;
```

```
% Constants
```

```

S = params(6);
L = params(2)*1e-3;
E = params(11)*1e-6;
lambda = params(3)*1e-9;
k = 2*pi/lambda;
f = params(1)*1e-3;
M2x = params(9);
M2y = params(10);
Dx = params(4)*1e-3;
Dy = params(5)*1e-3;
wox = (2.*lambda.*f.*M2x)/(pi.*Dx);
woy = (2.*lambda.*f.*M2y)/(pi.*Dy);
zox = params(7)*1e-3;
zoy = params(8)*1e-3;
zo = (pi*((wox+woy)/2)^2)/lambda;
zrx = (pi.*wox.^2)/(lambda.*M2x);
zry = (pi.*woy.^2)/(lambda.*M2y);
tau = params(12)*1e-15;
Io = (0.56*E)/(wox*woy*tau);
start = params(15)*1e-2;
finish = params(16)*1e-2;
pts = params(17);

```

```
% Theoretical Equation
```

```

for n = 1:pts
    z = start + (n-1)*(finish-start)/pts;
    sol(n) = beta(2)+((pi.*wox.*sqrt(1+((z+beta(3)-
zox).^2)./zrx.^2)).*woy.*sqrt(1+((z+beta(3)-
zoy).^2)./zry.^2)).*tau)/(2.*beta(1).*L.*(2.*log(1+sqrt(2))).*E)).*quad
(@(x)log(1+(beta(1).*L.*2.*log(1+sqrt(2))).*E.*(sech(x)).^2)/(pi.*wox.*
sqrt(1+((z+beta(3)-zox).^2)./zrx.^2)).*woy.*sqrt(1+((z+beta(3)-
zoy).^2)./zry.^2)).*tau)),-10,10);
end

```

```
% Function output
```

```

df = (data-sol).^2;
f = sqrt(sum(df(:)));

```

```

%%%%%%%%%%%%%%%%%%%%%%%%%%%%%%%%%%%%%%%%%%%%%%%%%%%%%%%%%%%%%%%%%%%%%%%%
% Geoffrey D. Jenkins - University of Dayton - WPAFB, OH - April 2008 %
%
% File name: n2fita.m
%
% This is the first of 2 m-files needed for performing automated
% curve fits to closed aperture z-scan data. This is the only file
% that needs to be run. It operates on the 2nd m-file, n2fitb.m,
% which needs to be in the same directory as this file.
% The code highlighted in yellow corrects the closed aperture data
% using the open aperture data and should be disabled if open
% aperture data does not exist.
%%%%%%%%%%%%%%%%%%%%%%%%%%%%%%%%%%%%%%%%%%%%%%%%%%%%%%%%%%%%%%%%%%%%%%%%

```

```

clear all
close all

```

```

guess = [1e-7*1e-4/1e9, 0, 0];

```

```

datafile = xlsread('BK7 - Closed - 0_75 mm - 10uJ');
global data2;
data2 = datafile(:,5)';
oadata = xlsread('BK7 OA 5uJ'); % For use with OA & CA Files
toa = oadata(:,5)'; % For use with OA & CA Files
global params;
params = datafile(:,6);

```

```

S = params(6);
global data;
data = data2+(1-toa).*((1-(1-S).^0.67)./S);
L = params(2)*1e-3;
E = params(11)*1e-6;
lambda = params(3)*1e-9;
k = 2*pi/lambda;
f = params(1)*1e-3;
M2x = params(9);
M2y = params(10);
Dx = params(4)*1e-3;
Dy = params(5)*1e-3;
wox = (2.*lambda.*f.*M2x)./(pi.*Dx);
woy = (2.*lambda.*f.*M2y)./(pi.*Dy);
zox = params(7)*1e-3;
zoy = params(8)*1e-3;
zo = (pi*((wox+woy)/2)^2)/lambda;
zrx = (pi.*wox.^2)./(lambda.*M2x);
zry = (pi.*woy.^2)./(lambda.*M2y);
tau = params(12)*1e-15;
Io = (0.56*E)/(wox*woy*tau);
start = params(15)*1e-2;
finish = params(16)*1e-2;
pts = params(17);

```

```

[n2,fval,eflag] =
fminsearch(@(n2)n2fitb(n2,data),guess,optimset('MaxFunEvals',50000,'Max
Iter',50000))

for n = 1:pts
    z = (start) + (n-1)*(finish-start)/pts;
    sol(n) = n2(3) + 1 + ((1-
S).^2.*(((z+n2(2))/zo).^2+3)./(((z+n2(2))/zo).^2+9)).*sin(-
(4.*((z+n2(2))/zo).*log(1-
S))./(((z+n2(2))/zo).^2+9)).*(k.*n2(1).*Io.*L))./(S.*(1+((z+n2(2))/zo)
.^2)));
end

dT = max(data)-min(data);
dphi = dT/(0.406*(1-S)^0.25);
zpeak = find(data==max(data));
zval = find(data==min(data));
if zpeak > zval
    n2calc = dphi/(k*L*Io);
else n2calc = -dphi/(k*L*Io);
end
phi = k*n2(1)*Io*L;
z = linspace(start,finish,pts);
plot(z*100,data,'*',z*100,sol)
hold all
plot(z*100,toa,'x',z*100,data2,'o')
set(gcf,'DefaulttextFontSize',8)
legend('Corrected Data','Fit','T_o_a','Data')
xlabel('Z-Position of Sample Relative to Focus (cm)')
ylabel('Normalized Transmission')
text(z(3)*100,(max(data)+0.15),['I_0 = ' num2str(Io/1e13) ' GW/cm^2'])
text(z(3)*100,(max(data)+0.15)-0.055,['L = ' num2str(L*1000) ' mm'])
text(z(3)*100,(max(data)+0.15)-0.11,['\tau = ' num2str(tau*1e15) ' fs
'])
text(z(3)*100,(min(data)-0.15)+0.11,['n_2 Fit = ' num2str(n2(1)*1e13) '
cm^2/GW'])
text(z(3)*100,(min(data)-0.15)+0.055,['n_2 Calc = '
num2str(n2calc*1e13) ' cm^2/GW'])
text(z(3)*100,(min(data)-0.15),['\Phi_0 = ' num2str(phi)])
text(z(3)*100,(max(data)+0.15)-0.165,['M^2(x) = ' num2str(M2x) ' ;
M^2(y) = ' num2str(M2y)])
text(z(3)*100,(min(data)-0.15)+0.165,['S = ' num2str(S)])
axis([start*100 finish*100 (min(data)-0.2) (max(data)+0.2)])

```

```

%%%%%%%%%%%%%%%%%%%%%%%%%%%%%%%%%%%%%%%%%%%%%%%%%%%%%%%%%%%%%%%%%%%%%%%%
% Geoffrey D. Jenkins - University of Dayton - WPAFB, OH - April 2008 %
%
% File name: n2fitb.m
%
% This is the 2nd of 2 m-files needed for performing automated
% curve fits to closed aperture z-scan data. This m-file is a
% function called by oafita.m
%%%%%%%%%%%%%%%%%%%%%%%%%%%%%%%%%%%%%%%%%%%%%%%%%%%%%%%%%%%%%%%%%%%%%%%%

function f = n2fitb(n2,data)

global params;

S = params(6);
L = params(2).*1e-3;
E = params(11).*1e-6;
lambda = params(3).*1e-9;
k = 2*pi/lambda;
f = params(1).*1e-3;
M2x = params(9);
M2y = params(10);
Dx = params(4).*1e-3;
Dy = params(5).*1e-3;
wox = (2.*lambda.*f.*M2x)/(pi.*Dx);
woy = (2.*lambda.*f.*M2y)/(pi.*Dy);
zox = params(7).*1e-3;
zoy = params(8).*1e-3;
zo = (pi*((wox+woy)/2)^2)/lambda;
zrx = (pi.*wox.^2)/(lambda.*M2x);
zry = (pi.*woy.^2)/(lambda.*M2y);
tau = params(12).*1e-15;
Io = (0.56*E)/(wox*woy*tau);
start = params(15).*1e-2;
finish = params(16).*1e-2;
pts = params(17);

% Theoretical Equation
for n = 1:pts
    z = start + (n-1)*(finish-start)/pts;
    sol(n) = n2(3) + 1 + ((1-
S).^(2.*(((z+n2(2))/zo).^2+3)./(((z+n2(2))/zo).^2+9)).*sin(-
(4.*((z+n2(2))/zo).*log(1-
S))./(((z+n2(2))/zo).^2+9)).*(k.*n2(1).*Io.*L))./(S.*(1+((z+n2(2))/zo)
.^2)));
end

% Function output
df = (data-sol).^2;
f = sqrt(sum(df(:)));

```

REFERENCES

- [1] S. Backus, C. G. Durfee III, M. M. Murnane, and H.C. Kapteyn, *High Power Ultrafast Lasers*, Rev. Sci. Instr. **69** No. 3, 1207-1223 (1997).
- [2] K. Okamoto, *Fundamentals of Optical Waveguides*, (Academic Press, San Diego, 2006): 200-203.
- [3] E. Puddu, A. Allevi, A. Andreoni, and M. Bondani, *All-optical logic operations by means of two interlinked $\chi^{(2)}$ interactions in a single crystal*, JOSA B **21** No. 10, 1839-1847 (2004).
- [4] B. E. A. Saleh, and M. C. Teich, *Fundamentals of Photonics* (John Wiley & Sons, Inc., United State of America, 1991): 740.
- [5] R. Adair, L. L. Chase, and S. A. Payne, *Nonlinear refractive-index measurements of glasses using three-wave frequency mixing*, Opt. Soc. Am. B **4** No. 6, 875-881 (1987).
- [6] M. P. Hasselbeck, *Nonlinear optics basics*, OPTC **00753**, 1-8 (2004).
- [7] Smith, Bechtel, and Bolenburg, *Dielectric breakdown thresholds and nonlinear index measurements with picoseconds pulses*, Physics Rev. B **12** No. 2 (1975).
- [8] M. Sheik-Bahae and M. P. Hasselbeck, *Third order optical nonlinearities*, OSA Handbook of Optics IV Ch. 17, 10 (2000).
- [9] B. E. A. Saleh, and M. C. Teich, *Fundamentals of Photonics* (John Wiley & Sons, Inc., United State of America, 1991): 181.
- [10] M. Sheik-Bahae, A. A. Said, and E. W. Van Stryland, *High sensitivity single beam n_2 measurements*, Opt. Lett. **14**, 955-957 (1989).
- [11] E. Hecht, *Optics*, (Addison-Wesley, 2001): 107
- [12] E. Hecht, *Optics*, (Addison-Wesley, 2001): 113
- [13] R. Adair, L. L. Chase, and S. A. Payne, *Nonlinear refractive index measurement of glasses using three-wave frequency mixing*, J. Opt. Soc. Am. B **4**, 875-881 (1987).

- [14] S. R. Friberg and P. W. Smith, *Nonlinear optical glasses for ultra-fast optical switches*, IEEE J. Quantum Electron. **QE-23**, 2089-2094 (1987).
- [15] M. J. Moran, C. Y. She, and R. L. Carman, *Interferometric measurements of nonlinear refractive-index coefficient relative to CS₂ in laser-system-related materials*, IEEE J. Quantum Electron. **QE-11**, 259-263 (1975).
- [16] Sheng-Li Guo, H. Wang, J. Yan, N. B. Ming, L. Xu, and X. Z. You, *Analytic method for the materials with nonlinear refraction and strong nonlinear absorption in Z-scan technique*, Proc. SPIE **4918**, 320-325 (2002).
- [17] S. M. Mian, B. Taheri, and J. P. Wicksted, *Effects of beam ellipticity on Z-scan measurements*, J. Opt. Soc. Am. **13**, No 5, 856-863 (1996).
- [18] P. Chen, D. A. Oulianov, I. V. Tomov, and P. M. Rentzepis, *Two-dimensional Z scan for arbitrary beam shape and sample thickness*, J. App. Phys. **85**, No. 10, 7043-7050 (1999).
- [19] J. A. Hermann, T. McKay, and R. G. McDuff, *Z-scan with arbitrary aperture transmittance: the strongly nonlinear regime*, Opt. Comm. **154**, 225-233 (1998).
- [20] P. Chen, I. V. Tomov, and P. M. Rentzepis, *A two dimensional Z-scan method for the measurement of optical nonlinear effects*, SPIE **3146**, 160-169 (1997).
- [21] A. Marcano O., H. Maillote, D. Gindre, and D. Metin, *Picosecond nonlinear refraction measurement in single-beam open Z scan by charge-coupled device image processing*, Opt. Lett. **21**, No 2, 101-103 (1996).
- [22] J. Wang, M. Sheik-Bahae, A. A. Said, D. J. Hagan, and E. W. Van Stryland, *Time-resolved Z-scan measurements of optical nonlinearities*, Opt. Soc. Am. B **11**, No. 6, 1009-1017 (1994).
- [23] T. Shimada, N. A. Kurnit, and M. Sheik-Bahae, *Measurement of nonlinear index by a relay-imaged top-hat Z-Scan technique*, SPIE **2714**, 52-60 (1996).
- [24] T. Bazaru, Ioan Dancus, P. S. Doia, A. Petris, and V. I. Vlad, *Multiple-pass z-scan for the characterization of the partial transparent nonlinear optical materials*, Proc. SPIE **5581**, 649-653 (2004).
- [25] G. Tsigaridas, M. Fakis, I. Polyzos, P. Persephonis, V. Giannetas, *Z-scan technique, through beam radius measurements*, Appl. Phys. B (2003).
- [26] D. G. McLean, P. A. Fleitz, and R. L. Sutherland, *New aspects in the interpretation of z-scan data*, SPIE **2853**, 74-83.

- [27] G. Tsigardis, M. Fakis, I. Polyzos, P. Persephonis, and V. Giannetas, *Z-scan technique through beam dimensions measurements*, Proc. SPIE **5131**, 24-28 (2003).
- [28] T. Xia, M. Sheik-Bahae, Z. Wang, A. A. Said, D. J. Hagan, and E. W. van Stryland, *EZ-scan: single beam measurement technique for thin-film nonlinearities*, SPIE **2229**, 148-156 (1994).
- [29] M. Mohebi, N. Jamasbi, A. Ruiz, *Measurement of the nonlinear refractive index of materials with a single pulse*, SPIE **3749**, 733-734 (1999).
- [30] T. Olivier, F. Billard, and H. Akhouayri, *Z-scan theoretical and experimental studies for accurate measurements of the nonlinear refractive index and absorption of optical glasses near damage threshold*, Proc. SPIE **5273**, 341-349 (2003).
- [31] E. Fazio, P. Bevilacqua, and M. Bertolotti, *Engineering of z-scan experimental configuration for fast characterization of nonlinear materials*, SPIE **2775**, 135-139 (1996).
- [32] M. Balu, L. A. Padilha, D. J. Hagan, E. W. Van Stryland, S. Yao, K. Belfield, S. Zheng, S. Barlow, and S. Marder, *Broadband z-scan characterization using a high-spectral-irradiance, high-quality supercontinuum*, Opt. Soc. Am. **25**, No. 2, 159-165 (2008).
- [33] M. Mohebi, N. Jamasbi, O. Morales, and Jesus Garduno, *Imaging-eclipsing-Z-scan method for measurement of the nonlinear refractive index of materials*, SPIE **3572**, 236-239 (1999).
- [34] F. Billard, T. Olivier, and H. Akhouayri, *Study and experimental setting of the z-scan method for accurate nonlinear refractive index and absorption metrology*, Proc. SPIE **5273**, 334-340 (2003).
- [35] X. Liu, S. Guo, H. Wang, and L. Hou, *Theoretical study on the closed-aperture Z-scan curves in the materials with nonlinear refraction and strong nonlinear absorption*, Opt. Comm. **197**, 431-437 (2001).
- [36] P. B. Chapple, J. Staromlynska, J. A. Hermann, T. J. McKay, and R. G. McDuff, *Single-beam z-scan: measurement techniques and analysis*, J. NL Opt. Phys. And Mat'l. **6**, No. 3, 251-293 (1997).
- [37] W. Zhao, J. H. Kim and P. Palffy-Muhoray, *Proc. SPIE* **2229**, 131-147 (1994).
- [38] J.C. Lagarias, J. A. Reeds, M. H. Wright, and P. E. Wright, *Convergence Properties of the Nelder-Mead Simplex Method in Low Dimensions*, SIAM Journal of Optimization **9**, No. 1, 112-147 (1998).

- [39] R. L. Sutherland, *Handbook of Nonlinear Optics* (Marcel Dekker, Inc., New York, 2003), second edn.
- [40] G. L. Desautels, *Reference Values*, AFRL Ultrafast lab (2005).
- [41] K. Kamada, *Mechanisms of ultrafast refractive index change in organic system*, Proc. SPIE **4797**, 65-75 (2003).
- [42] Schott, *Optical glass data sheets*, (Schott North America Inc., 2007): 11.
- [43] E. W. Weisstein, *Standard Deviation*, Mathworld,
<http://mathworld.com/standarddeviation.html>, 2008.
- [44] M. J. Therien, *Unpublished reference materials*, WPAFB, 2008.

R00259382C